

SU(2) gauge theory with one and two adjoint fermions towards the continuum limit

Andreas Athenodorou,^{1,*} Ed Bennett,^{2,†} Georg Bergner,^{3,‡} Pietro Butti,^{4,5,§} Julian Lenz,^{2,6,¶} and Biagio Lucini^{7,**}

¹*Computation-based Science and Technology Research Center,
The Cyprus Institute, 20 Kavafi Str., Nicosia 2121, Cyprus*

²*Swansea Academy of Advanced Computing, Swansea University, Fabian Way, Swansea SA1 8EN, UK*

³*University of Jena, Institute for Theoretical Physics, Max-Wien-Platz 1, D-07743 Jena, Germany*

⁴*Departamento de Física Teórica, Facultad de Ciencias and Centro de Astropartículas y Física de Altas Energías (CAPA),
Universidad de Zaragoza, Calle Pedro Cerbuna 12, E-50009, Zaragoza, Spain*

⁵*Instituto de Física Teórica UAM-CSIC, Nicolás Cabrera 13–15,
Universidad Autónoma de Madrid, Cantoblanco, E-28049 Madrid, Spain*

⁶*Helmholtz Zentrum Dresden Rossendorf, Bautzner Landstraße 400, 01328 Dresden, Germany*

⁷*Department of Mathematics, Swansea University, Fabian Way, Swansea SA1 8EN, UK*

(Dated: August 2, 2024)

We provide an extended lattice study of the SU(2) gauge theory coupled to one Dirac fermion flavour ($N_f = 1$) transforming in the adjoint representation as the continuum limit is approached. This investigation is supplemented by numerical results obtained for the SU(2) gauge theory with two Dirac fermion flavours ($N_f = 2$) transforming in the adjoint representation, for which we perform numerical investigations at a single lattice spacing value, which is analysed together with earlier calculations. The purpose of our study is to advance the characterisation of the infrared properties of both theories, which previous investigations have concluded to be in the conformal window. For both, we determine the mass spectrum and the anomalous dimension of the fermion condensate using finite-size hyperscaling of the spectrum, mode number analysis of the Dirac operator (for which we improve on our previous proposal) and the ratio of masses of the lightest spin-2 particle over the lightest scalar. All methods provide a consistent picture, with the anomalous dimension of the condensate γ_* decreasing significantly as one approaches the continuum limit for the $N_f = 1$ theory towards a value consistent with $\gamma_* = 0.174(6)$, while for $N_f = 2$ the anomalous dimension decreases more slowly with β . A chiral perturbation theory analysis show that the infrared behaviour of both theories is incompatible with the breaking of chiral symmetry.

CONTENTS

		H. R ratio	17
I. Introduction	1	IV. Conclusions	20
II. Summary of the continuum and lattice theory	3	Acknowledgments	21
III. Results	4	References	21
A. Expectation value of Polyakov loops and center symmetry	5		
B. Topological aspects	6		
C. Glueball Masses	7		
D. Torelon masses and the string tension	9		
E. States involving fermions	9		
F. Determination of the mass anomalous dimension	10		
1. Finite-size hyperscaling of particle spectrum	10		
2. γ_* from the mode number of the Dirac operator	10		
3. γ_* in the continuum limit	14		
G. Comparison with chiral perturbation theory	16		

I. INTRODUCTION

Large anomalous dimensions have been advocated in beyond the Standard Model strong dynamics to reconcile the proposed fundamental mechanism of electroweak symmetry breaking with experimental observations. A primary example is provided by *walking technicolor*, whereby a large anomalous dimension of the chiral condensate would explain the suppression of flavour-changing neutral currents [1–7]. An additional case in point is partial top compositeness in a theory in which the Standard Model Higgs boson is originated by the global symmetry breaking in a novel strong interaction [8–10]. In the case of such a Composite Higgs model, a large anomalous dimension of the chimera baryon (a baryon-like composite state containing fermions in the fundamental and in a two-index representation) is needed to enhance the mass of the top quark to the electroweak scale (see., e.g., [11–14]). Large anomalous dimensions are expected to appear in non-Abelian gauge theories

* a.athenodorou@cyi.ac.cy

† e.j.bennett@swansea.ac.uk

‡ georg.bergner@uni-jena.de

§ pbutti@unizar.es

¶ j.lenz@hzdr.de

** b.lucini@swansea.ac.uk

near the onset of the conformal window, a phase in which the theory is approximately scale-invariant in the infrared. The opening of the conformal window is determined by the structure and the size of the gauge group, and by the fermion content of the model (specifically, the gauge group representations under which the fermion matter fields transform and the number of fermion flavours in each representation). The onset of the conformal window being a strong coupling problem, analytically only semi-quantitative estimates are possible (see, e.g., [15–20]).

As for other non-perturbative questions in non-Abelian Quantum Field Theories, numerical simulations of the relevant model(s) discretised on a spacetime lattice provide in principle a robust framework to investigate the infrared conformal regime and its onset, enabling us to access crucial quantities such as the value of the anomalous dimension itself. Triggered by the experimental activity that led to the discovery and the characterisation of the Higgs boson [21, 22], the resurgent interest in understanding whether strongly interacting systems beyond the Standard Model can provide a viable fundamental mechanism of electroweak symmetry breaking has spawned a significant number of lattice studies aimed at unveiling the phase diagram of gauge theories for given group families and fermion representations in terms of the size of the gauge group and the number of flavours in each representation (see, e.g., Refs. [23–44] and Refs. [45–65] for a necessarily incomplete set of investigations targeting the problem of near-conformality respectively in the context of walking technicolour and top partial compositeness). To this purpose, a number of methods aimed at determining with sufficient accuracy the anomalous dimension of relevant operators or the (scheme-dependent) coupling at which the theory is infrared conformal have been proposed and studied. Among them, popular approaches include hyperscaling, dilaton perturbation theory, scaling of the eigenvalues of the Dirac operator, Schrödinger functional, and the gradient flow. Some relevant references to this body of work include [66–72], with relevant reviews provided for instance in [61, 73–78].

While strongly interacting theories beyond the Standard Model provide a clear-cut phenomenological motivation to study near-conformality, the underlying question of the possible phase structure of gauge theories is more fundamental and wider-reaching. The existence of an asymptotically free confined phase and of a Coulomb phase can be inferred directly from the sign of the β -function as a function of the gauge group size and structure, of the number of flavours and of the representation of the gauge group under which the latter transforms, including cases in which fermions transforming in different representations are present. The higher end of the conformal window, before the loss of asymptotic freedom, can be exposed in perturbation theory, giving rise to the well-known Banks-Zaks infrared fixed point [79, 80]. Outside perturbation theory, the conformal window is well understood in the presence of a high degree of super-

symmetry [81], which imposes strong constraints to the β -function. In non-supersymmetric quantum field theory, lattice calculations remain the most robust method to investigate the lower end of the conformal window, in which strong coupling plays a crucial role.

In this paper, we investigate two well-known gauge models, both based on gauge group $SU(2)$, coupled respectively with one and two fermions transforming in the adjoint representation of the gauge group, with the aim of providing further insides on their infrared behaviour and investigate quantitatively the value of the anomalous dimension in the continuum limit. The system with number of fermionic flavours $N_f = 2$, whose physical relevance relies on the observation that it could provide a minimal template for a realisation of walking technicolour, has been studied systematically for well over a decade on the lattice, using a wide array of methods. The consensus reached is that the system is infrared conformal with a small anomalous dimension, which exclude it from the class of phenomenologically relevant models. However, a robust determination of the anomalous dimension is still lacking. Tensions in the obtained data are shown for instance in [42].

The system with $N_f = 1$ has been considered in the context of semiclassical analysis [82] and volume independence, leading to the conjecture of emergent fermion symmetry also in the non-supersymmetric case [83]. A numerical study of this system was first provided by some of us in Ref. [39], where it was shown that, despite common lore, the system is not in the expected confining and chiral symmetry breaking phase; moreover, albeit at fixed lattice spacing, this study was the first to determine an order one anomalous dimension for the chiral condensate, which would fulfill one of the requirements of walking technicolour. Subsequent analytic work based on 't Hooft anomaly matching [84–88] showed that the model has an interesting phase structure in which topology plays a key role. An interesting observation made in [84] is the emergence of a light composite fermion in the spectrum. Subsequent numerical studies [44, 89] have confirmed that the system does not have the conventional properties of a confining and chiral symmetry breaking theory. However, while more likely, the near-conformal scenario has not proved to provide a striking fit to the data. Additionally, the expected light fermion in the spectrum has not been observed, and the anomalous dimension has been found to have a strong dependency on the lattice spacing. In contrast to earlier results, a recent study based on an overlap lattice action [90] favours rather a chiral symmetry breaking scenario. This lattice formulation provides an improved representation of the continuum symmetries, but so far the considered lattices have been rather coarse. A similar result might be deduced from the study of a mixed adjoint-fundamental theory [91] with Wilson clover fermions, but again the parameter range has been very limited. Finally, the system with $N_f = 1$ includes only two Goldstone bosons resulting from the breaking of chiral symmetry. This makes

it phenomenologically unviable to account for the standard model electroweak symmetry breaking. However, the system can be extended to a physically viable setup through the ultra minimal walking technicolor (UMWT) model [92], which also includes fermions in the fundamental representation.

The current status of understanding of these two models calls for additional simulations on larger lattices, closer to the continuum and to the chiral limit. In alignment with this demand, the purpose of our work is to extend the numerical results of previous investigations in order to provide a more solid understanding of the infrared dynamics of the target models. Therefore, we provide a range of new numerical results for SU(2) gauge theories with $N_f = 1$ and $N_f = 2$ adjoint fermion flavours at larger couplings, larger lattices and smaller masses. For continuity with our previous studies, we employ the Wilson action for the gauge part of the models, and we use the standard Wilson discretisation of fermions. This simple discretization allows us achieve very large lattice sizes at small fermion masses and combine a large set of data in our final analysis that include also those produced in previous investigations. We aim to get to the maximum point that can be achieved with our current approach. At the same time we want to investigate to what extend the same uncertainties that we have observed for $N_f = 1$ also appear in case of the seemingly well investigated $N_f = 2$ theory. The main tools we employ for the characterisation of the model are the behaviour of the chiral condensate, the scaling of the mass spectrum and the scaling of the eigenvalues of the Dirac operator.

The rest of the paper is organised as follows. In Sec. II we provide a quick overview of the continuum theories of interest and their lattice counterpart employed in this work. Sec. III is dedicated to a discussion of the methodology and the extraction of the main results, with different physical observables of interest discussed in different subsections. Conclusions can be found in Sec. IV. Preliminary results of our study have already appeared in [93].

II. SUMMARY OF THE CONTINUUM AND LATTICE THEORY

The Lagrangian of the SU(2) gauge theory with N_f adjoint Dirac flavours in Minkowski space, is defined as:

$$\mathcal{L} = -\frac{1}{2}\text{Tr}(G_{\mu\nu}(x)G^{\mu\nu}(x)) + \sum_{\alpha=1}^{N_f} \bar{\psi}_\alpha(x) (i\mathcal{D} - m) \psi_\alpha(x), \quad (1)$$

with $\mathcal{D} = (\partial_\mu + igA_\mu(x))\gamma^\mu$, γ_μ being the Dirac matrices, $A_\mu(x) = \sum_a T^a A_\mu^a(x)$ with $a = 1, 2, 3$, and the T_a the Lie algebra generators of SU(2) in the adjoint representation. The field strength tensor is defined as $G_{\mu\nu} = \partial_\mu A_\nu(x) - \partial_\nu A_\mu(x) + ig[A_\mu(x), A_\nu(x)]$, with g being the gauge coupling of the theory, and the trace is

taken over the gauge group. Notation and conventions are explained in Ref. [39].

We may re-express each Dirac flavour $\psi_\alpha(x)$ in terms of two Majorana flavours $\xi_{\alpha\pm}(x)$, by making use of the projections

$$\xi_{\alpha+} = \frac{\psi_\alpha + C\bar{\psi}_\alpha^T}{\sqrt{2}}, \quad \xi_{\alpha-} = \frac{\psi_\alpha - C\bar{\psi}_\alpha^T}{\sqrt{2}i}, \quad (2)$$

such that

$$\psi_\alpha = \frac{1}{\sqrt{2}}(\xi_{\alpha+} + i\xi_{\alpha-}). \quad (3)$$

Eq. (1) may then be re-expressed as

$$\mathcal{L} = -\frac{1}{2}\text{Tr}(G_{\mu\nu}(x)G^{\mu\nu}(x)) + \frac{1}{2} \sum_{\alpha=1}^{N_f} \sum_{k \in \{+, -\}} \bar{\xi}_{\alpha k}(x) (i\mathcal{D} - m) \xi_{\alpha k}(x), \quad (4)$$

exposing the SU($2N_f$) chiral symmetry in the action. The adjoint representation being real, the expected chiral symmetry breaking pattern is

$$\text{SU}(2N_f) \mapsto \text{SO}(2N_f). \quad (5)$$

In this work, we consider the cases $N_f = 1, 2$. We use the same computational setup as our previous work [44]: we generate dynamical gauge configurations using the standard Wilson plaquette action and the standard Wilson fermion action

$$S = S_G + S_F, \quad (6)$$

where

$$S_G = \beta \sum_p \text{Tr} \left[1 - \frac{1}{2} U(p) \right], \quad (7)$$

$$S_F = \sum_{x,y} \bar{\psi}(x) D(x,y) \psi(y), \quad (8)$$

N_f is the number of flavours, $U(p)$ is the traced parallel transport of the links $U_\mu(x)$ around a plaquette p , and $D(x,y)$ is the Wilson Dirac operator

$$D(x,y) = \delta_{x,y} - \kappa [(1 - \gamma_\mu) U_\mu(x) \delta_{y,x+\mu} + (1 + \gamma_\mu) U_\mu^\dagger(x - \mu) \delta_{y,x-\mu}]. \quad (9)$$

For full details we refer the reader to Ref. [44]. This generation is performed using importance sampling methods: the Hybrid Monte Carlo (HMC) [94] algorithm for $N_f = 2$, and RHMC [95] for $N_f = 1$. A change from our previous work is the software used to perform these algorithms: while for heavier ensembles we continue to make use of HiRep [34, 96], for lighter ensembles we use Grid [97, 98], which enables significantly more powerful

TABLE I. Ensembles used for the $N_f = 1$ theory, $\beta \leq 2.15$, showing the name of the ensemble, the coupling β , the bare fermion mass am , the number of sites in the temporal and spatial directions N_t and N_s , and the total number of configurations considered.

	β	am	$N_t \times N_s^3$	$N_{\text{conf.}}$
DB1M1	2.05	-1.475	32×16^3	4000
DB1M1*	2.05	-1.475	24×12^3	4000
DB1M2	2.05	-1.49	32×16^3	4000
DB1M3	2.05	-1.5	24×12^3	4000
DB1M4	2.05	-1.51	48×24^3	4000
DB1M4*	2.05	-1.51	32×16^3	4163
DB1M4**	2.05	-1.51	24×12^3	4013
DB1M5	2.05	-1.514	32×16^3	4000
DB1M6	2.05	-1.519	32×16^3	4000
DB1M7	2.05	-1.523	48×24^3	4000
DB1M7*	2.05	-1.523	32×16^3	4000
DB1M8	2.05	-1.524	48×24^3	4000
DB1M8*	2.05	-1.524	32×16^3	4006
DB1M9	2.05	-1.5246	48×24^3	4000
DB2M1	2.1	-1.42	24×12^3	4000
DB2M2	2.1	-1.43	24×12^3	4000
DB2M3	2.1	-1.44	24×12^3	4000
DB2M4	2.1	-1.45	32×16^3	4000
DB2M5	2.1	-1.46	32×16^3	4000
DB2M6	2.1	-1.47	48×24^3	4000
DB2M6*	2.1	-1.47	40×20^3	4000
DB2M7	2.1	-1.474	64×32^3	4000
DB3M1	2.15	-1.35	24×12^3	4000
DB3M2	2.15	-1.36	24×12^3	4000
DB3M3	2.15	-1.37	24×12^3	4000
DB3M4	2.15	-1.38	32×16^3	4100
DB3M5	2.15	-1.39	32×16^3	4077
DB3M6	2.15	-1.4	32×16^3	4014
DB3M7	2.15	-1.41	48×24^3	4000
DB3M8	2.15	-1.422	48×24^3	4000

GPU-based resources to be used.¹ Computation of specific observables using these configurations is discussed in the relevant subsections of the next section.

III. RESULTS

In the following sections we provide an overview of the main results obtained at a wide range of lattice volumes, masses, and coupling constants, as summarised in Tables I, II, and III. An investigation explaining why we have chosen these parameters to avoid the bulk phase and retrieve the desired continuum physics can be found in our previous investigations [39, 44]. In this work the parameter range is significantly larger than in any previous

TABLE II. Ensembles used for the $N_f = 1$ theory, $\beta \geq 2.2$, showing the name of the ensemble, the coupling β , the bare fermion mass am , the number of sites in the temporal and spatial directions N_t and N_s , and the total number of configurations considered.

	β	am	$N_t \times N_s^3$	$N_{\text{conf.}}$
DB4M1	2.2	-1.28	24×12^3	8000
DB4M2	2.2	-1.29	24×12^3	4320
DB4M3	2.2	-1.3	32×16^3	4000
DB4M3*	2.2	-1.3	24×12^3	4000
DB4M4	2.2	-1.31	32×16^3	4000
DB4M4*	2.2	-1.31	24×12^3	4000
DB4M5	2.2	-1.32	32×16^3	4000
DB4M5*	2.2	-1.32	24×12^3	4000
DB4M6	2.2	-1.33	24×12^3	4092
DB4M7	2.2	-1.34	32×16^3	4000
DB4M7*	2.2	-1.34	24×12^3	4000
DB4M8	2.2	-1.35	32×16^3	4000
DB4M9	2.2	-1.36	48×24^3	4000
DB4M9*	2.2	-1.36	32×16^3	4000
DB4M9**	2.2	-1.36	24×12^3	4000
DB4M10	2.2	-1.37	48×24^3	4000
DB4M11	2.2	-1.378	48×24^3	4000
DB4M12	2.2	-1.386	64×32^3	4226
DB4M13	2.2	-1.39	96×48^3	4049
DB5M1	2.25	-1.22	24×12^3	4000
DB5M2	2.25	-1.24	24×12^3	4000
DB5M3	2.25	-1.26	24×12^3	4000
DB5M4	2.25	-1.28	32×16^3	4000
DB5M4*	2.25	-1.28	24×12^3	4000
DB5M5	2.25	-1.3	32×16^3	4000
DB5M5*	2.25	-1.3	24×12^3	4000
DB5M6	2.25	-1.31	32×16^3	4000
DB5M7	2.25	-1.32	32×16^3	4000
DB5M8	2.25	-1.33	32×16^3	4000
DB6M1	2.3	-1.16	32×16^3	4000
DB6M1*	2.3	-1.16	24×12^3	4000
DB6M2	2.3	-1.18	32×16^3	4000
DB6M2*	2.3	-1.18	24×12^3	4000
DB6M3	2.3	-1.2	32×16^3	4000
DB6M3*	2.3	-1.2	24×12^3	4000
DB6M4	2.3	-1.22	32×16^3	4000
DB6M5	2.3	-1.24	32×16^3	4000
DB6M5*	2.3	-1.24	24×12^3	4000
DB6M6	2.3	-1.26	32×16^3	4000
DB6M6*	2.3	-1.26	24×12^3	4000
DB6M7	2.3	-1.28	48×24^3	4000
DB6M7*	2.3	-1.28	32×16^3	4000
DB6M8	2.3	-1.304	64×32^3	4285
DB6M9	2.3	-1.31	96×48^3	4141
DB7M1	2.4	-1.1	32×16^3	4000
DB7M2	2.4	-1.12	32×16^3	4000
DB7M3	2.4	-1.14	32×16^3	4000
DB7M4	2.4	-1.16	32×16^3	4000
DB7M5	2.4	-1.18	32×16^3	4000
DB7M6	2.4	-1.2	32×16^3	4000
DB7M7	2.4	-1.21	48×24^3	4090
DB7M8	2.4	-1.222	48×24^3	4702
DB7M9	2.4	-1.234	64×32^3	4000
DB7M10	2.4	-1.243	96×48^3	1736

¹ In each case minor modifications were made to the base code referenced above. In the case of HiRep, these are available in the `su2nf1adj` branch of the fork at <https://github.com/edbennett/HiRep>, commit 6632758. In the case of Grid, they are in the `su2nf1adj_dirac13` branch of the fork at https://github.com/edbennett/Grid_epcc, commit 48ca3a2.

TABLE III. Ensembles used for the $N_f = 2$ theory, showing the name of the ensemble, the coupling β , the bare fermion mass am , the number of sites in the temporal and spatial directions N_t and N_s , and the total number of configurations considered. Only $\beta = 2.35$ ensembles are shown: data presented in this work for $\beta = 2.25$ were obtained from previous work; no new ensembles were generated nor measurements performed at this β .

	β	am	$N_t \times N_s^3$	$N_{\text{conf.}}$
Nf2DB2M1	2.35	-0.9	32×16^3	4001
Nf2DB2M2	2.35	-0.95	32×16^3	4001
Nf2DB2M3	2.35	-1.0	48×24^3	4001
Nf2DB2M5	2.35	-1.05	64×32^3	4086
Nf2DB2M6	2.35	-1.09	96×48^3	4309
Nf2DB2M6*	2.35	-1.09	64×32^3	4332
Nf2DB2M7	2.35	-1.11	128×64^3	4428
Nf2DB2M7*	2.35	-1.11	96×48^3	3945

work. In fact, in this work we have pushed the boundary of computational feasibility with the chosen approach.

Our main goal is to include in particular the dependence on the gauge coupling β . The large parameter space requires first some general considerations to avoid a breaking of center symmetry indicated by the Polyakov loop or topological freezing. Afterwards we present the results for the scaling of the particle spectrum and the mass anomalous dimension.

A. Expectation value of Polyakov loops and center symmetry

On a finite lattice with compact directions, when the direction μ is large enough, the model is characterised by a linear realisation of the four center symmetries

$$\mathbb{Z}_\mu(2) : U_\mu(x) \rightarrow (1 - 2\delta_{x_\mu, \hat{x}_\mu}) U_\mu(x), \quad (10)$$

which multiplies by $z = -1$ all the links $U_\mu(x)$ in the lattice slice identified by the fixed μ -th coordinate $x_\mu = \hat{x}_\mu$. Here, \hat{x}_μ is a conventionally fixed value.

The $\mathbb{Z}_\mu(2)$ symmetries can be spontaneously broken at small volumes, signaling severe finite-size effects. To verify that the finite lattice extent has not caused the centre symmetry of the group to be broken, we compute the expectation value of the Polyakov loop

$$P_\mu = \frac{1}{N} \sum_{x_\perp} \text{Tr} \left(\prod_{i=0}^{L_\mu-1} U_\mu(x_\perp, x_i) \right). \quad (11)$$

A broken centre symmetry would be indicated by two peaks in the histogram of this observable, while the preserved symmetry shows a single peak centered at $\langle P_\mu \rangle = 0$. We show a sample of such histograms in Fig. 1. In all cases we observe this symmetry to be unbroken.

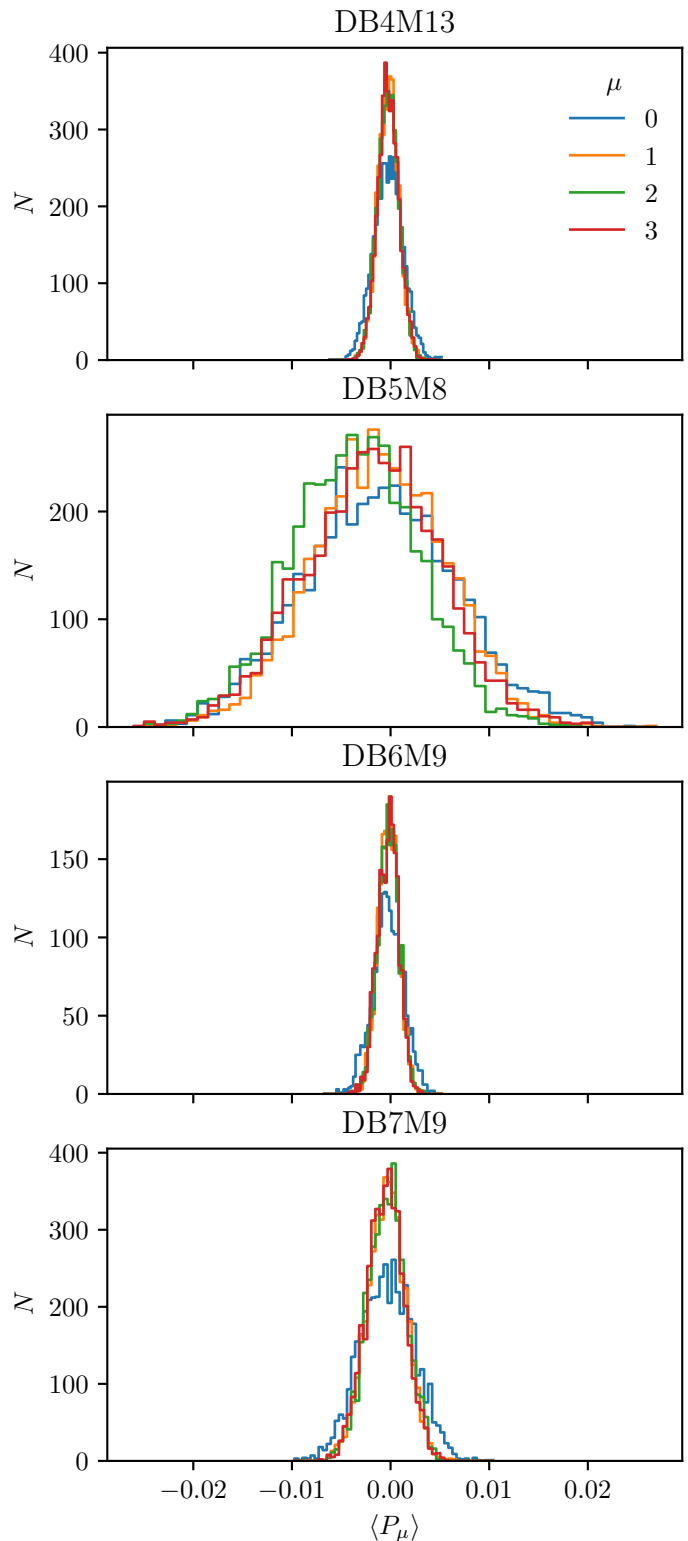


FIG. 1. Polyakov loop histograms, for the ensembles DB4M13, DB5M8, DB6M9, and DB7M9.

B. Topological aspects

The formal definition of the topological charge [99, 100] for a gauge field is given by the four-dimensional Euclidean integral of the topological density across space-time:

$$Q = \frac{1}{32\pi^2} \int d^4x \epsilon_{\mu\nu\rho\sigma} \text{Tr} [G_{\mu\nu}(x)G_{\rho\sigma}(x)]. \quad (12)$$

In practical terms, any appropriate lattice discretization of the topological charge density that results in the correct continuum expression can be employed to assess the lattice equivalence. Using the standard clover representation of the topological charge density, Eq. (12) takes the summation form:

$$Q_L = \frac{1}{32\pi^2} \sum_x \epsilon_{\mu\nu\rho\sigma} \text{Tr} [C_{\mu\nu}(x)C_{\rho\sigma}(x)], \quad (13)$$

where $C_{\mu\nu}(x)$ is the standard cloverleaf discretization of the gauge field tensor $G_{\mu\nu}(x)$:

$$\begin{aligned} C_{\mu\nu}(x) = & \frac{\text{Im}}{4} \left[U_\mu(x)U_\nu(x+a\hat{\mu})U_\mu^\dagger(x+a\hat{\nu})U_\nu^\dagger(x) \right. \\ & + U_\nu(x)U_\mu^\dagger(x-a\hat{\mu}+a\hat{\nu})U_\nu^\dagger(x-a\hat{\mu})U_\mu(x-a\hat{\mu}) \\ & + U_\mu^\dagger(x-a\hat{\mu})U_\nu^\dagger(x-a\hat{\mu}-a\hat{\nu})U_\mu(x-a\hat{\mu}-a\hat{\nu})U_\nu(x-a\hat{\nu}) \\ & \left. + U_\nu^\dagger(x-a\hat{\nu})U_\mu(x-a\hat{\nu})U_\nu(x+a\hat{\mu}-a\hat{\nu})U_\mu^\dagger(x) \right]. \quad (14) \end{aligned}$$

An issue lattice simulations of gauge theories face is the development of significant correlations among topological sectors at reaching the continuum limit. This phenomenon, known as topological freezing, occurs because the probability distribution for the creation of instantons and anti-instantons from the vacuum is suppressed as the continuum limit is approached [44]. Consequently, the total topological charge cannot fluctuate adequately, causing the Markov chain to become trapped in specific topological sectors. Consequently, the simulation might fail to thoroughly explore every topological sector efficiently and thus be ergodic. In practice, as the continuum limit is approached, pronounced correlations emerge and contribute to an increment of the necessary number of configurations needed to attain statistically significant vacuum expectation values for physical observables.

This issue is a common obstacle in all Markov-chain algorithms where updates are performed locally. To investigate whether this phenomenon occurs for the values of β chosen in our work, we have closely observed the autocorrelation time of the topological charge in our simulation runs.

Monte Carlo assessments of the topological charge Q encounter challenges due to ultraviolet fluctuations that obscure the inherent topological structure. To address this issue, smoothing techniques like gradient flow [101] can be applied to mitigate these fluctuations.

Regarding our simulations for $N_f = 1$, in Fig. 2, we illustrate the Monte Carlo evolution of the topological charge Q for the ensembles DB4M13, DB5M8, DB6M9,

and DB7M10 along with their respective histograms. For DB4M13 DB6M9, and DB7M10 we provide histories for three different threads of configuration production.

These above four sets of configurations correspond to the smallest fermion masses at the four largest values of β . It is noticeable that none of the ensembles exhibit an exceptionally long autocorrelation time for the topological charge Q , indicating that topological freezing is not a concern within the specified parameter range. The simulations explore a substantial number of topological sectors, and the resulting histograms align well with a Gaussian distribution centered at zero. This strongly suggests an effective sampling of topological observables.

Turning now to the case of $N_f = 2$, in Fig. 3 we present the Monte Carlo histories of the topological charge Q for the ensembles Nf2DB2M6 and Nf2DB2M7 along with their corresponding histograms. Once more, these two sets of configurations refer to the smallest masses as well as to the largest possible volumes. Clearly, and in contrast to the case of $N_f = 1$, the topological charge appears to fluctuate infrequently indicating large auto-correlation times and suppressed ergodicity. As a result, Q probes only a few topological sectors. Bearing in mind that the sampling is not ideal as we move towards smaller masses for $N_f = 2$ and $\beta = 2.35$ we should be cautious of any low-ergodicity effects contaminating our measurements. Detailed findings concerning the autocorrelation time and the fitted form of the Q histogram are provided in the data release associated with this work [102].

In addition to verifying the reliability of the simulations, this study also offers additional insights into the physical properties of the theory. The topological susceptibility χ defined as

$$\chi = \frac{\langle Q^2 \rangle - \langle Q \rangle^2}{V}, \quad (15)$$

provides information regarding the potential infrared conformal scenario for the theory. When an infrared (IR) conformal theory is deformed by a fermion mass, it transitions to a confining phase. In this case, the theory should behave similarly to the equivalent quenched theory. A suitable quantity to verify this scenario is the topological susceptibility, as it should align with the results of pure SU(2) Yang–Mills theory [103].

In Fig. 4, we display the topological susceptibility in units of the string tension, $\chi^{\frac{1}{4}}/\sqrt{\sigma}$, as a function of the string tension in lattice units, $a^2\sigma$ for both SU(2) with $N_f = 1$ and $N_f = 2$ adjoint fermions. The results are compared to the corresponding quantity in pure SU(2) Yang–Mills theory for the quenched $N_f = 0$ ($am \rightarrow \infty$) case. The topological susceptibility for $N_f = 1$ and $\beta \neq 2.4$, for $N_f = 2$ excluding the very first two points for $\beta = 2.35$ show good agreement among these three theories, with any discrepancies attributed to higher-order scaling corrections of $a^2\sigma$. Clearly, for $N_f = 1$ and $\beta = 2.4$, the topological susceptibility exhibits large negative deviations as we approach $a^2\sigma \rightarrow 0$, which are understood as underestimated values attributed to critical

slowing down. Similarly, the same phenomenon occurs for $N_f = 2$ at $\beta = 2.35$ for the two smallest values of $a^2\sigma$.

In addition, the gradient flow facilitates the establishment of scale parameters, namely, t_0 and w_0 , which can be determined with a high degree of precision using the following prescription: first, set $\mathcal{E}(t)$ as

$$\mathcal{E}(t) = t^2 \langle E(t) \rangle \quad \text{where} \quad E(t) = \frac{1}{4} B_{\mu\nu}^2(t). \quad (16)$$

In this expression $B_{\mu\nu}$ represents the field strength derived from flowing $G_{\mu\nu}$. We designate the scale t_0 as the specific value of t at which the following identification occurs:

$$\mathcal{E}(t)|_{t=t_0(c)} = \mathcal{E}_0. \quad (17)$$

In a similar manner we define w_0 in the following way:

$$t \frac{d}{dt} \mathcal{E}(t)|_{t=w_0^2(c)} = \mathcal{W}_0. \quad (18)$$

In the above definitions, the parameters \mathcal{E}_0 and \mathcal{W}_0 are selected to ensure that the pertinent condition, either $a \ll \sqrt{8t_0} \ll L$ or $a \ll \sqrt{8w_0} \ll L$, is fulfilled. Choosing a small value of c tends to result in larger lattice artifacts, while larger c typically leads to increased autocorrelations [104]. In our specific scenario, we set c to 0.2, aligning with the common choice of $c = 0.3$ in QCD, assuming a scaling with N as described in Ref. [51]. $G_{\mu\nu}$ is computed via the clover plaquette $C_{\mu\nu}$.

C. Glueball Masses

Glueball masses can be determined by employing the standard decomposition method on a Euclidean correlator that incorporates an operator referred to as $\phi(t)$ [105]. This decomposition procedure hinges on expressing these physical states in the framework of the Hamiltonian, designated as H , and its corresponding energy eigenstates:

$$\begin{aligned} \langle \phi^\dagger(t = an_t) \phi(0) \rangle &= \langle \phi^\dagger e^{-H an_t} \phi \rangle \\ &= \sum_i |c_i|^2 e^{-aE_i n_t} \\ &\stackrel{t \rightarrow \infty}{\equiv} |c_0|^2 e^{-aE_0 n_t}. \end{aligned} \quad (19)$$

In the above context, E_0 signifies the ground state energy. The summation mentioned is constrained to states with non-zero overlaps, satisfying the condition $c_i = \langle \text{vac} | \phi^\dagger | i \rangle \neq 0$. The quantum characteristics of the operator ϕ must align with those of the specific state under examination; i.e., glueball states. Identifying the ground state relies on two crucial factors: the strength of its correlation with the state created by ϕ and the rate of exponential decay, as indicated in Eq. (19). Improving this correlation involves devising operators that effectively capture the essential traits of the state. To enhance the overlap onto the states under investigation,

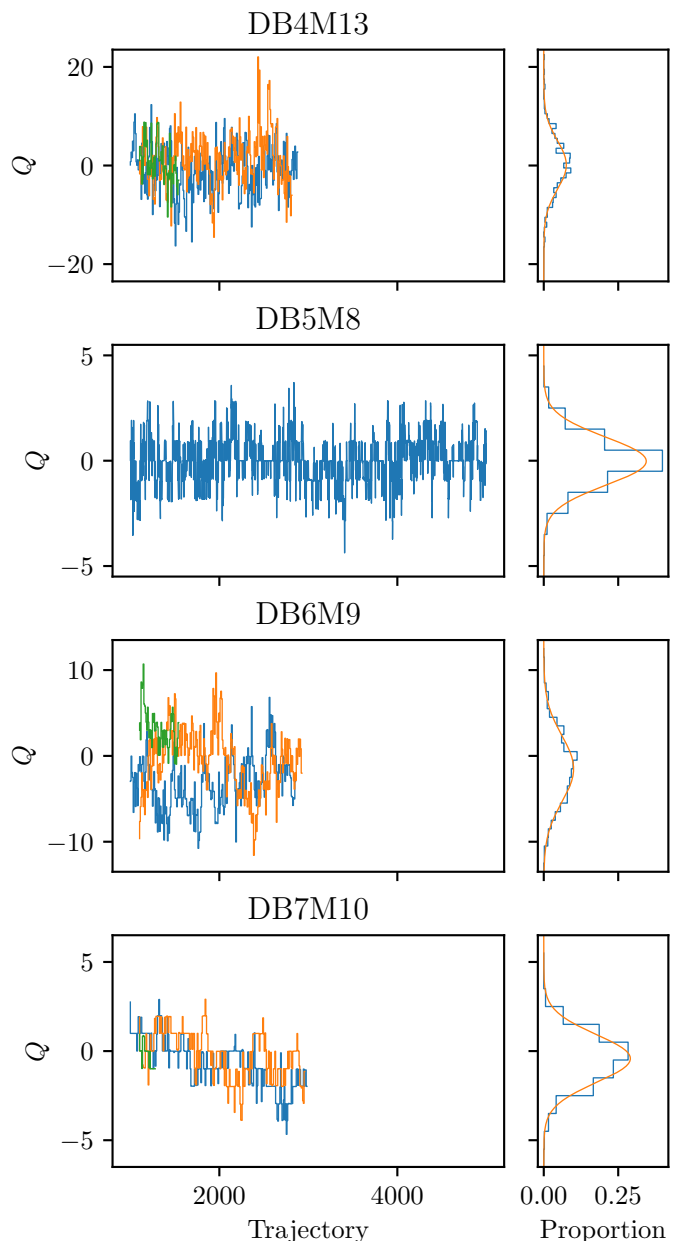


FIG. 2. Topological charge histories (left), and histograms (right), for the ensembles DB4M13, DB5M8, DB6M9, and DB7M10.

the GEVP technique [106–108] is employed on a set of operators ϕ_i derived from various lattice loops at different blocking levels [109, 110]. This process utilizes correlation matrices, denoted as $C_{ij} = \langle \phi_i^\dagger(t) \phi_j(0) \rangle$, where $i, j = 1, \dots, N_{\text{op}}$, in conjunction with GEVP. Here, N_{op} represents the number of operators used.

To formulate an operator projecting onto a glueball state, we generate an ordered product of SU(2) link matrices along a loop that allows continuous contraction, followed by the calculation of its trace. The real (imaginary) part of this trace corresponds to positive (negative)

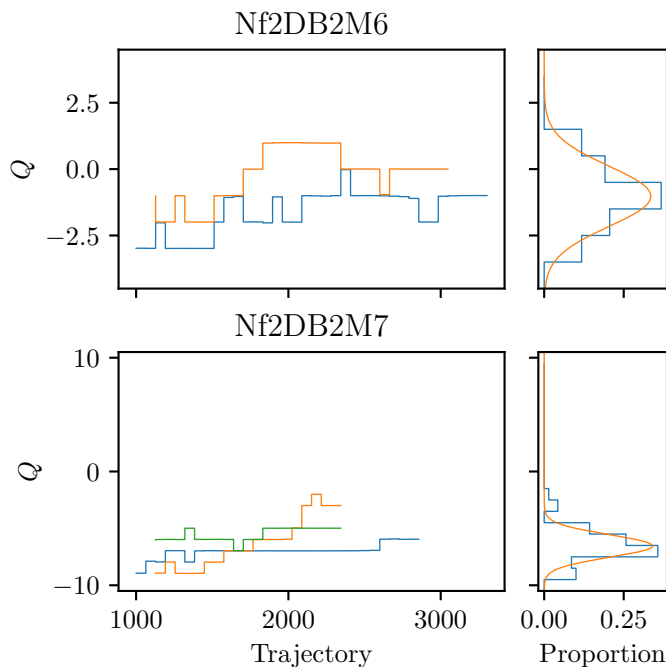


FIG. 3. Topological charge histories (left), and histograms (right), for the ensembles Nf2DB2M6 and Nf2DB2M7.

charge conjugation $C = +(-)$. To ensure the operator possesses zero momentum, we sum over all spatial translations of the loop. Additionally, we consider all possible rotations of the loop, combining them in manners consistent with the irreducible representations (\mathcal{R}) of the rotational symmetry group. For the creation of operators with both parities ($P = \pm$), we construct the parity inverse for each loop and then combine them in appropriate linear combinations. In Fig. 5, we present a selection of the paths utilized in building our basis.

The distinct representations R of the discrete subgroup of cubic rotations within the complete rotation group are labeled as A_1, A_2, E, T_1, T_2 . The A_1 representation is a singlet and exhibits complete cubic rotational symmetry, encompassing the $J = 0$ state in the continuum limit. Similarly, the A_2 representation is also a singlet. The E representation constitutes a doublet, while both T_1 and T_2 representations are triplets. In the lattice context, the three states corresponding to the triplet of T_1 and T_2 are degenerate. To address this, their values are averaged, treating them as a single state when estimating glueball masses. The same approach is applied to the E doublets, where their mass estimates are averaged.

The rotational symmetry representations outlined above are rooted in our cubic lattice formulation. As we approach the continuum limit, these states will converge to continuum glueball states falling into representations of continuous rotational symmetry. Consequently, they will form degenerate multiplets comprising $2J + 1$ states, where J denotes the spin of the states. When determining the continuum limit of the low-lying glueball spec-

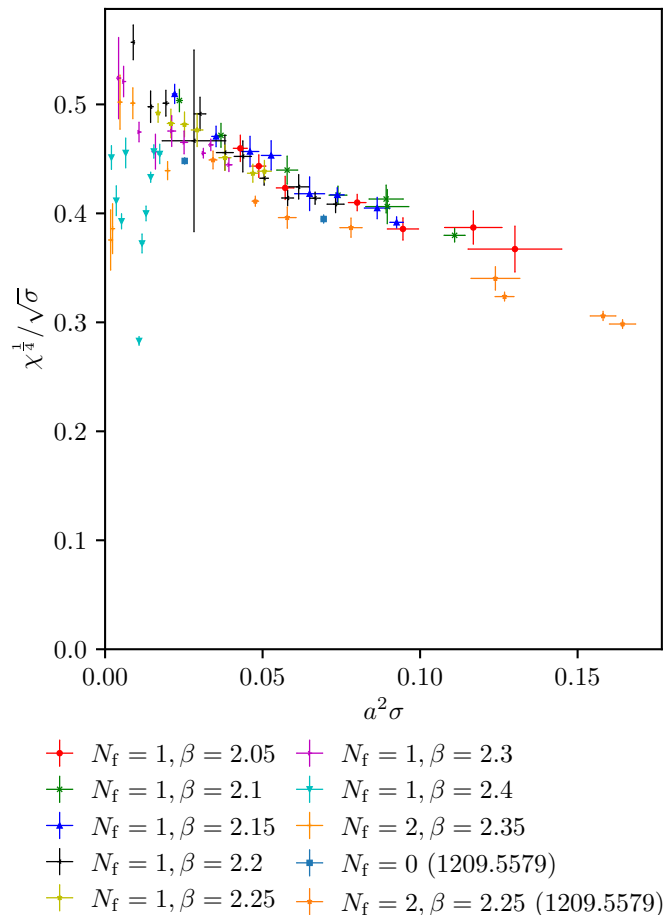


FIG. 4. The topological susceptibility as a function of the string tension for the $N_f = 1$ and 2 ensembles presented in this work, compared with data from previous work for the quenched theory and $N_f = 2, \beta = 2.25$ [103].

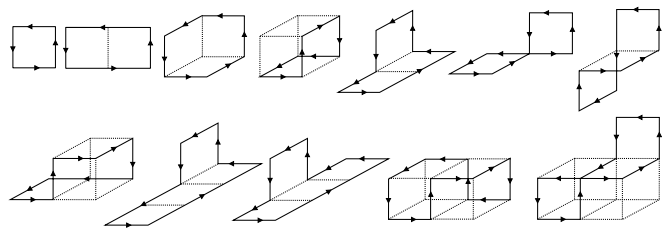


FIG. 5. All the different paths used for the creation of the glueball operators

trum, it is more informative to assign states to a specific spin J instead of representations of the cubic subgroup. The latter provides a less precise “resolution,” as it maps all spins $J = 1, 2, 3, \dots, \infty$ to just 5 cubic representations. For low values of J ($J = 0, 1, 2$), the distribution of the $2J + 1$ states can be characterized as $A_1 \rightarrow J = 0$, $T_1 \rightarrow J = 1$, and $E, T_2 \rightarrow J = 2$.

D. Torelon masses and the string tension

Similar to the glueball mass calculation, we can determine the mass of the closed spatial Polyakov loop, also known as a torelon, which wraps around a compactified spatial direction. Torelon states are characterized by quantum numbers such as angular momentum-spin J , transverse parity P_{\perp} , and longitudinal parity P_{\parallel} . The ground state, with $J^{P_{\perp}, P_{\parallel}}=0^{++}$, allows for the easiest extraction of the string tension [111].

The mass of the torelon is determined by computing the ground state energy $m_T(L)$ of a flux-tube with length $L = N_s$, which forms a closed loop by winding once around a spatial compactified torus. We utilize Eq. (19), where the operator ϕ represents the product of SU(2) link matrices along a non-contractible closed path, which wraps around the spatial torus once. We use the most basic form of such an operator, the elementary Polyakov loop. This is the path-ordered product of link matrices in a spatial direction, winding once around the torus along the aforementioned spatial direction. Once again, we utilize smearing and blocking techniques to improve the projection onto physical states. We also sum over translations along the spatial-torus as well as over the transverse directions within the time slice to project onto zero longitudinal and transverse momentum, respectively. As all spatial lattice extents are identical, we average the correlation function over the three spatial directions.

Confining torelons, exhibit behavior resembling that of bosonic strings [111]. It is expected that the closed flux-tube behaves akin to a confining bosonic string, whose spectrum can be approximated with reasonable accuracy by the Nambu-Goto string model [112]. The ground state mass of the closed bosonic string is described by the expression:

$$m_T(l) = \sigma l \sqrt{1 - \frac{2\pi}{3\sigma l^2}}. \quad (20)$$

Here, σ represents the string tension and $l = aL$ indicates the length of the torelon. Therefore, we calculate the string tension across the torelon mass spectrum. Results for the string tension are shown in Fig. 6.

E. States involving fermions

Mesons and baryons are sourced by operators of the form

$$O(x) = \bar{\psi}(x)\Gamma\psi(x), \quad (21)$$

where Γ is a product of Dirac γ matrices giving the symmetry of interest. As discussed above, this theory has a chiral symmetry breaking pattern $SU(2N_f) \rightarrow SO(2N_f)$, and we choose to label the states observed in these terms. The remaining subgroup SO(2) in case of $N_f = 1$ is equivalent to $U(1)$ (refer to as $U(1)$ baryon symmetry). For convenience, in Table IV we summarise this convention.

TABLE IV. A summary of the nomenclature used for meson symmetry channels in this work, including the interpolating operator used to access each channel, the quantum numbers under the U(1) baryon symmetry and parity, and the name we use to refer to the state in the theories presented here. (The vector meson, marked *, is in fact accessible from the connected correlation function, as the disconnected contribution is identically zero.)

Γ	$U(1)^P$	Name
$\gamma_5, \gamma_0\gamma_5$ singlet	0^-	Pseudoscalar meson
1 triplet	$\pm 2^-$	Pseudoscalar (anti)baryon
1, γ_0 singlet	0^+	Scalar meson
$\gamma_5, \gamma_0\gamma_5$ triplet	$\pm 2^+$	Scalar (anti)baryon
$\gamma_5\gamma_k, \gamma_0\gamma_5\gamma_k$ singlet	0^+	Axial vector meson
$\gamma_k, \gamma_0\gamma_k$ singlet*	0^-	Vector meson
$\gamma_5\gamma_k$ triplet	$\pm 2^-$	Vector (anti)baryon

Similarly to the case for glueballs above, correlation functions of these operators converge at large time to an exponential decay with the ground state mass in the exponent

$$\langle O_X^\dagger(t)O_X(0) \rangle \stackrel{t \rightarrow \infty}{\approx} f_X \cdot e^{-m_X t}, \quad (22)$$

where m_X and f_X are the ground state mass and decay constant of the state sourced by $O_X(x)$. In a finite volume with antiperiodic boundary conditions, this then becomes

$$\langle O_X^\dagger(t)O_X(0) \rangle \stackrel{t \rightarrow \infty}{\approx} f_X \left[e^{-m_X t} + e^{-m_X(T-t)} \right], \quad (23)$$

Inverting Eq. (23) defines an effective mass m_{eff} , and by finding where m_{eff} has a plateau at large time, we may identify the region that is free from the effect of excited states. We then fit the correlator to Eq. (23) to obtain the mass and decay constant of the state.

Additionally, as the bare Wilson fermion mass acquires an additive renormalisation, we define a renormalised fermion mass—the PCAC mass—via the axial Ward identity [113].

In this work we continue to use HiRep to implement the computation of correlation functions. The fits are performed using the `pyerrors` [114] library, which computes uncertainties using the Γ method [115], automatically accounting for autocorrelations in the data.

One particular difference to theories in the fundamental representation is the appearance of bound states formed out of gluons combined with an adjoint fermion field. One particular of these states is a spin- $\frac{1}{2}$ field (also called hybrid fermion, and denoted as \check{g} in plots), which corresponds to the so-called gluino-gluon field in $\mathcal{N} = 1$ supersymmetric Yang-Mills theory. The corresponding operator is

$$O(x) = \sum_{\mu\nu} \sigma_{\mu\nu} \text{Tr} [F^{\mu\nu}(x)\lambda(x)], \quad (24)$$

where $\sigma_{\mu\nu} = \frac{1}{2} [\gamma_\mu, \gamma_\nu]$, the field strength is represented by a clover plaquette and smearing is applied to improve the signal. Further details of the techniques can be found in corresponding publications of supersymmetric Yang-Mills theory [116]. This correlation function is computed separately from the spectrum of mesons and baryons using the FlexLatSim code [117], but analysed with the same workflow using `pyerrors`.

We present the spectrum of masses and decay constants respectively of the $N_f = 1$ theory, including mesons, baryons, glueballs, the string tension, and the hybrid fermion, in Figs. 6 and 8, in terms of the gradient flow scale w_0 . For the case $N_f = 2$, we present the spectrum in terms of the string tension $\sqrt{\sigma}$ in Fig. 7; in this case we do not use w_0 , as in the majority of ensembles the lattice extent is insufficient to extract it.

In particular, we draw attention to two features of the spectrum. The first, highlighted in Fig. 9, is that, as observed in our previous work and in other theories in or near the conformal window, the scalar glueball is lighter than the 2^+ scalar baryon, the would-be pion in a QCD-like theory. Indeed, this effect becomes more pronounced at higher values of β . Secondly, as can be seen in Fig. 10, in the $N_f = 2$ theory the spin- $\frac{1}{2}$ state is also lighter than the 2^+ scalar baryon.

F. Determination of the mass anomalous dimension

1. Finite-size hyperscaling of particle spectrum

In a mass-deformed conformal theory in a finite volume, we expect the masses M of states to hyperscale with the deforming mass (which we approximate by m_{PCAC}) and the lattice extent L as

$$LaM = f \left(L (am_{\text{PCAC}})^{\frac{1}{1+\gamma_*}} \right). \quad (25)$$

While we do not *a priori* know the functional form of $f(L(am_{\text{PCAC}}))$, we may look for a value of γ_* that causes the data to collapse onto a single universal curve. As in Ref. [44], we may make this determination more systematic by defining the curve collapse as the minimisation of the function

$$P(\gamma_*) = \frac{1}{N_o} \sum_{\ell \in \{L\}} \sum_{i \in S_\ell} \left(L_i a M_i - f_\ell \left(L_i^{1+\gamma_*} a m_{\text{PCAC}} \right) \right)^2, \quad (26)$$

where $\{L\}$ is the set of lattice extents, S_ℓ is the set of data having lattice extent $L_i \neq \ell$ but lying such that $L_i^{1+\gamma_*}$ is in the range spanned by data with lattice extent ℓ , N_o is the number of points summed over, and f_ℓ is an interpolating function across the data having lattice extent ℓ , which we choose to be piecewise linear. We apply this procedure for the data for each value of β in both $N_f = 1$ and 2.

The results of this analysis are plotted for a selection of β values considered for $N_f = 1$ in Fig. 11 and for $N_f = 2$

TABLE V. Results for the values for γ_* obtained for $N_f = 1$ both by fitting the spectrum with a finite-size hyperscaling Ansatz, and by fitting the Dirac mode number. The mode number has not been fitted for the case $\beta = 2.25$, due to the absence of larger-volume ensembles in that case.

β	γ_* (FSHS)	N_{points}	γ_* (AIC)	Ensemble
2.05	0.926(68)	13	0.848(16)(16)	DB1M8
			0.878(15)(16)	DB1M9
2.1	0.89(12)	4	0.7009(66)(75)	DB2M7
2.15	0.777(47)	7	0.671(36)(21)	DB3M8
2.2	0.693(30)	23	0.589(15)(15)	DB4M11
			0.5359(16)(13)	DB4M13
2.25	0.69(11)	4
2.3	0.587(19)	8	0.4468(14)(24)	DB6M9
2.4	0.498(19)	13	0.3892(34)(29)	DB7M7
			0.3843(13)(11)	DB7M10

TABLE VI. Results for the values for γ_* obtained for $N_f = 2$ both by fitting the spectrum with a finite-size hyperscaling Ansatz, and by fitting the Dirac mode number.

β	γ_* (FSHS)	N_{points}	γ_* (AIC)	Ensemble
2.25	0.426(13)	100
2.35	0.3332(61)	10	0.3042(39)(109)	Nf2DB2M6

in Fig. 12, and the resulting values of γ_* tabulated in Tabs. V and VI respectively. As observed in our previous work [44], we see the anomalous dimension in the $N_f = 1$ theory continue to decrease as β increases; for $N_f = 2$ we obtain $\gamma_* = 0.3042(39)(109)$ from the analysis of the mode number, which is only moderately smaller than the result $\gamma_* = 0.371(20)$ obtained previously using similar techniques [70] for $\beta = 2.25$.

2. γ_* from the mode number of the Dirac operator

The other method we employ to calculate the mass anomalous dimension is studying the low-lying mode number of the Dirac operator. A similar computation to extract γ_* was performed in previous publications [39, 44], to which we will refer to for additional details. However, the final analysis of the data has been improved and follows a slightly different strategy. For this reason, it is useful to review some general concepts, that will be useful in the following as they will guide the statistical analysis of the data.

The quantity of interest is the dependence of the spectral density ρ of the Dirac operator on its eigenvalues ω . In fact, in an infrared conformal gauge theory, at the IR fixed point, the leading behaviour of $\rho(\omega)$ is dictated by the renormalization group (RG) equations and proves to be power-like in ω , where the anomalous dimension γ^* appears as an exponent [70]. Equivalently, a more accessible quantity is the integral of the spectral density,

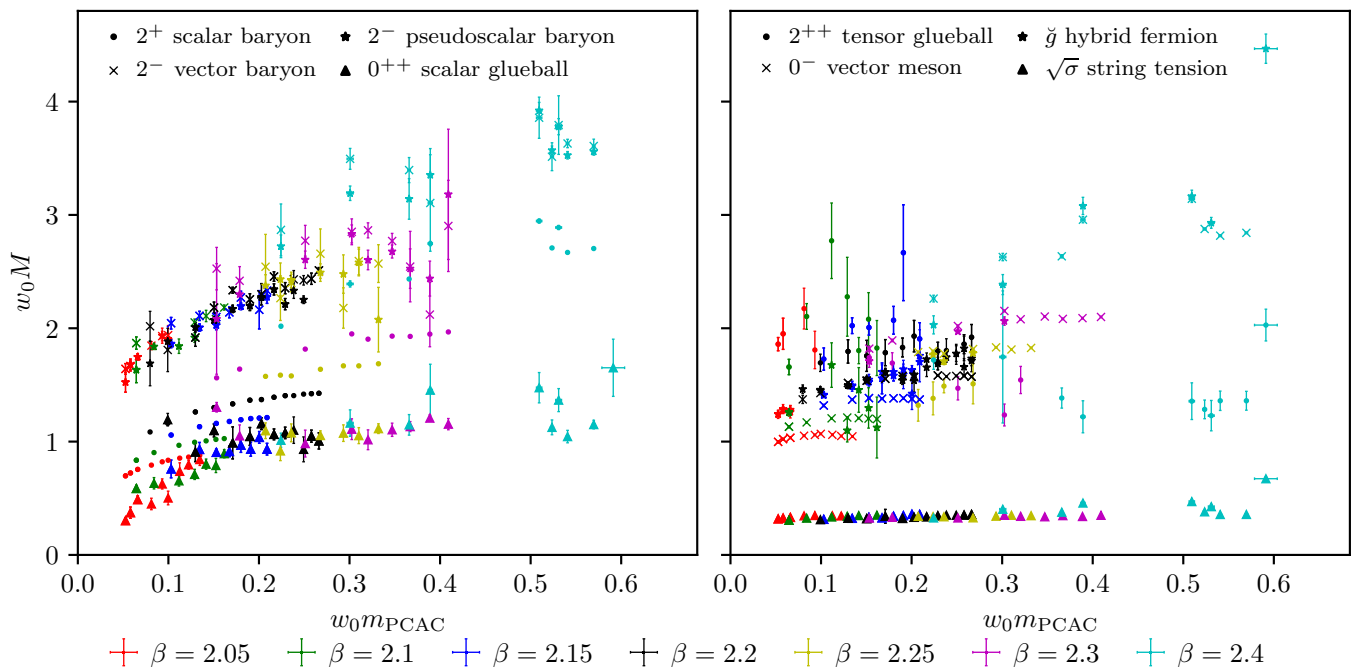


FIG. 6. Spectrum of particle masses in the $N_f = 1$ theory, scaled by the gradient flow scale w_0 .

called *mode number*, i.e. the number of eigenvalues of the Dirac operator lower than a certain mass threshold Ω^2 (divided by the volume). As argued in Refs. [70, 118], on the lattice, the mode number in lattice units $a^{-4}\bar{\nu}$, can be expressed as a function of the threshold $a\Omega$ as

$$a^{-4}\bar{\nu}(\Omega) \approx a^{-4}\bar{\nu}_0(m) + A[(a\Omega)^2 - (am)^2]^{-\frac{2}{1+\gamma^*}}. \quad (27)$$

where $a^{-4}\bar{\nu}_0$, A , am and γ^* are parameters to be fitted to the data. In Eq. (27), the \approx sign signals the fact that the equation is valid only where the dynamics is dominated by the IR fixed point, namely a region $\omega_{\text{IR}} < \omega < \omega_{\text{UV}}$ of low eigenvalues insensitive to the fermion mass. The parameters appearing in Eq. (27) are of physical relevance and contain information that can be incorporated into the analysis of the data. Specifically:

- The overall additive constant $\bar{\nu}_0$ represents the integral of the spectral density in the region $[0, \omega_{\text{IR}}]$, where the fermion mass drives the theory away from the IR fixed points, spoiling scale invariance. In this region, no analytical models are available for ρ , and therefore its integral is represented by a constant $\bar{\nu}_0$. As the fermion mass is responsible for this behaviour, this region shrinks in the chiral limit, and, as argued in Ref. [70], it can be parameterized as

$$\bar{\nu}_0(m) \propto M^4 \quad (28)$$

where M is some mass in the spectrum vanishing in the chiral limit.

- The mass parameter m can be related to the bare PCAC mass as

$$m = Z_A m_{\text{PCAC}}. \quad (29)$$

The procedure for the extraction of the anomalous dimension consists of the following. First, the mode number $\bar{\nu}$ has to be computed through spectral projection and the Chebyshev expansion method as described in [42]. We have confirmed consistency between both methods and the main part of the results has been obtained with the Chebyshev expansion. This provides the mode number for several values of the threshold $a\Omega$ on a subsample of well-decorrelated configurations. Then a fit of Eq. (27) to the data has to be performed to extract the value of the anomalous dimension γ^* . In doing so two main issues have to be addressed.

The first issue is the choice of the window $[a\Omega_{\text{min}}, a\Omega_{\text{max}}]$. This range is expected to reflect the region of validity of Eq. (27) and its location is not known *a priori* and has to be determined empirically from the data. In principle, when choosing an inappropriate window, i.e. a region where Eq. (27) is not valid, the low quality of the choice of $a\Omega_{\text{min}}$ and $a\Omega_{\text{max}}$ is expected to be signalled by a bad- χ^2 fit. In practice, the usage of the simple χ^2 as an indicator of the quality of the fit is not always a good discriminator. In fact, if the window is small enough and centred on high eigenvalues, the fit converges with a good χ^2 to unphysical values of the parameters.²

² As pointed out in Ref. [70], the spectral density has an asymp-

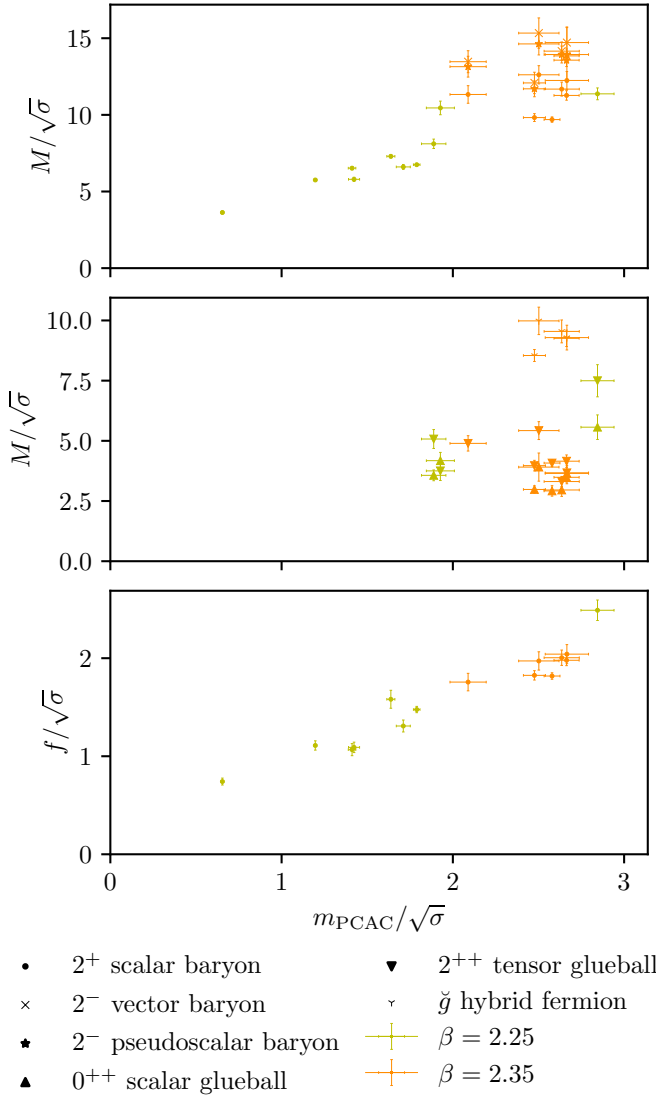


FIG. 7. Spectrum of particle masses and decay constants in the $N_f = 2$ theory, scaled by the string tension $\sqrt{\sigma}$.

For this reason, fits in a low-eigenvalues window are to be preferred, although a second following issue is expected to be triggered; the high degree of non-linearity of the function in Eq. (27) makes the fit highly unstable, the minimization algorithm often drives towards a region in the parameter space where $((a\Omega)^2 - (am)^2) < 0$ and leads to a breakdown of the fitting procedure. In these cases, the fit parameters can be bounded or reparameterized to avoid this problem, although, we observed that in some cases the algorithm finds other local minima, and the parameters converge to extreme (unphysical) values.

otic behaviour dominated by asymptotic freedom, given by $\rho \propto \omega^3$. If the fitting region is small enough, the fit of Eq. (27) to the data can give an acceptable χ^2 , leading to a vanishing value of am and a γ^* with no physical meaning.

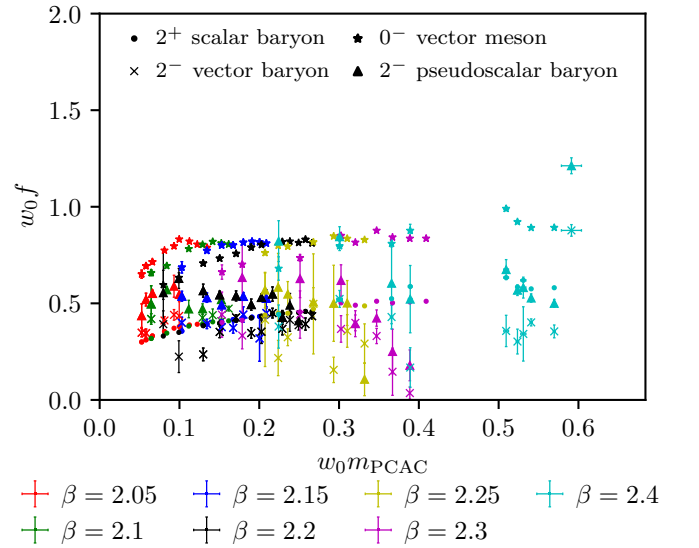


FIG. 8. Spectrum of decay constants in the $N_f = 1$ theory, scaled by the gradient flow scale w_0 .

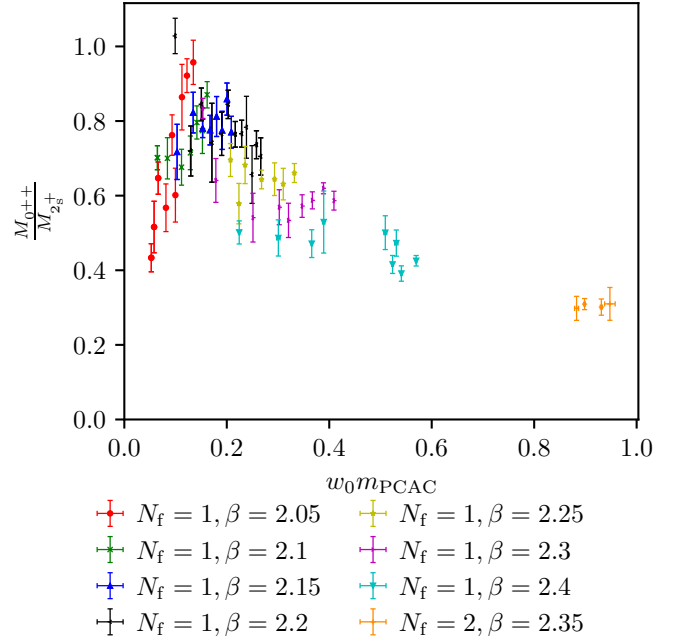


FIG. 9. Ratio of the mass of the scalar glueball to the lightest fermionic bound state in both the $N_f = 1$ and $N_f = 2$ theories.

In previous publications [39, 44], these two issues were dealt with by repeating a series of bootstrapped fit to an extensive range of possible window $[a\Omega_{\min}, a\Omega_{\max}]$ and thus seeking by eye for a region of stability. Coefficients were then extracted by averaging over the windows inside the stability region, where its fit is weighted with the relative portion of converged fit in a bootstrap sample, as an indicator of stability. In this work, we adopt a different approach, which reduces the number of arbitrary choices in the analysis and frames the procedure within

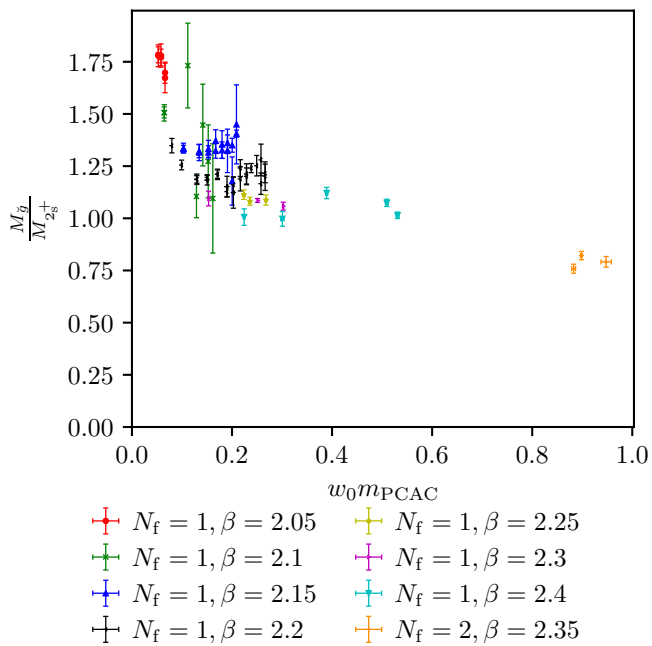


FIG. 10. Ratio of the mass of the to the lightest fermionic bound state in both the $N_f = 1$ and $N_f = 2$ theories.

a more solid statistical framework. To address the problem of the stability of the fit, we constrain fit parameters to physically reasonable ranges by means of Bayesian constraints with Gaussian priors [119]. The procedure consists in the minimization of the *augmented chi-square* $\chi_{\text{aug}}^2 = \chi^2 + \chi_{\text{pr}}^2$, defined as

$$\chi^2(\mathbf{p}) = \sum_{i,j} [\nu_i - f_i(\mathbf{p})] C_{ij}^{-1} [\nu_j - f_j(\mathbf{p})], \quad (30)$$

where the index i runs over all the data points within the fitting window, ν_i represents the mode number data computed on the lattice for a specific mass threshold $a\Omega_i$, $f_i(\mathbf{p})$ corresponds to the model function in Eq. (27) applied to a specific value of $a\Omega_i$ within the window for given values of the parameter vector $\mathbf{p} = [a^{-4}\bar{\nu}_0, A, am, \gamma^*]$, and C is the full covariance matrix estimated from the Monte-Carlo data. In addition to that, we consider uncorrelated Gaussian priors for the parameters $\tilde{p}_n, \tilde{\sigma}_{p_n}$ that contribute to the global loss function as

$$\chi_{\text{pr}}^2(\mathbf{p}, \{\tilde{p}_n, \tilde{\sigma}_{p_n}\}) = \sum_{n=1}^4 \frac{(p_n - \tilde{p}_n)^2}{\tilde{\sigma}_{p_n}^2}. \quad (31)$$

The selection of their central value is performed in a *physics-informed* way. Following Eq. (29), the prior of am is centred to the value of am_{PCAC} defined in Sec. III E times a coefficient which we set to 1.³ On the base of

Eq. (28), the prior of $a^{-4}\bar{\nu}_0$ is centred to the lattice estimate of the (fourth power of the) scalar baryon mass times a coefficient of order 1. The priors for A and γ^* are set to 1(10) and 0.5(5.0), respectively. It is to be stressed that priors are only meant to improve the convergence of the fit as they supposedly prevent the minimization algorithm from being stuck in some local minimum. The choice of their numerical values should not influence the final result. To ensure the validity of this assumption, as it is common in this Bayesian framework, the width of the prior should be made large enough to accommodate significant fluctuations from the central value, i.e. choosing a so-called *flat* prior. Following this criterion, the widths of the priors are set to account for a 1000% relative error in the choice of the central values of γ^* and A 's priors, 100% for am and $a^{-4}\bar{\nu}_0$. In order to ensure the positivity of $a^{-4}\bar{\nu}_0$ and am , we use a log-normal distribution for their prior. We repeat the constrained fit for a large number of possible windows by varying $a\Omega_{\text{min}} \in [0.03, 0.1]$ and $a\Omega_{\text{max}} \in [0.08, 0.18]$. As an example of the results of the fit, in Fig. 13 we display the anomalous dimension γ^* extracted from a fit, as a function of the parameters $a\Omega_{\text{min}}$ and $a\Omega_{\text{max}}$ for the ensemble DB4M11 in a three-dimensional space with coordinates $(a\Omega_{\text{max}}, a\Omega_{\text{min}}, \gamma^*)$. In order to seek a stable region in an automatized way, we calculate the gradient of the surface generated by our γ^* value and we filter those points in which the norm of the gradient is below a certain threshold, in order to automatize the identification of the stable region. In the upper panel of Fig. 13 we assign a colder colour to those points whose gradient is smaller, i.e. corresponding to a “flatter” and therefore stabler region. The final result has to be given by averaging the coefficients over the different fitting windows in the stable region. This last scenario is analogous to the issue of *data truncation* arising in other contexts such as hadron spectroscopy in lattice QCD. In the last few years, *Bayesian model averaging* techniques to address this problem have started to raise a lot of interest [120–122], and have been used in several published results. Similar to our case, the goal is to address the problem of the selection of a subset of data for a fit and avoid being overly conservative in the estimation of the systematic error, by re-formulating the problem as a *model selection* problem. Our proposal is to apply the methodology suggested in [120] by assigning to each window a so-called (modified) Akaike information criteria (AIC), defined as

$$\text{AIC} = \chi_{\text{aug}}^2(\mathbf{p}^*) + 2N_{\text{cut}} \quad (32)$$

where $\chi_{\text{aug}}^2(\mathbf{p}^*)$ is the augmented chi-square for the “best-fit” parameters \mathbf{p}^* and N_{cut} is the number of available points minus the number of points in the fit.⁴ A weight factor $w = e^{-\text{AIC}/2}$ is then assigned in the final average

³ This coefficient should correspond to the renormalization factor Z_A . We do not have a determination, but we assume it to be of order 1.

⁴ In Ref. [120], the weight factor differs for an extra factor k in the exponent, k being the number of parameters in the fitting

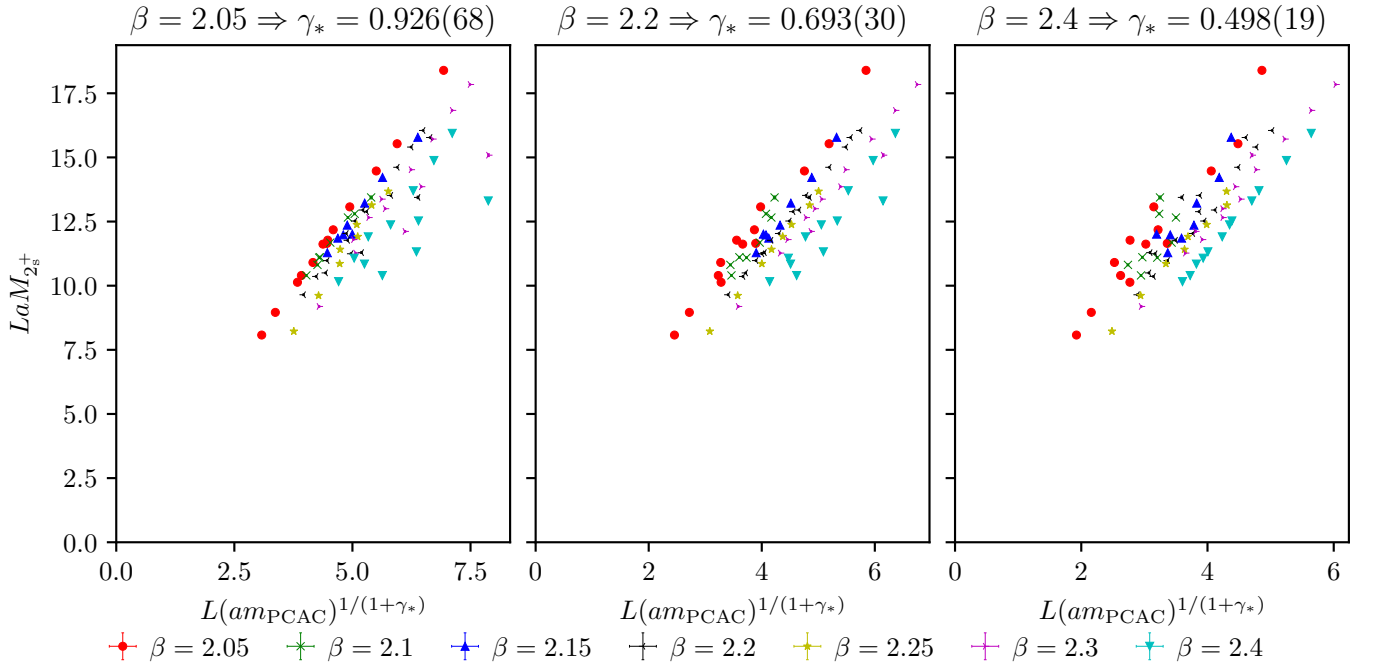


FIG. 11. Finite-volume hyperscaling fit results for $N_f = 1$. In each panel, the value of γ_* used for the horizontal co-ordinate is that obtained from the FSHS fit of the data at a single value of β , as indicated above the plot. Data from the remaining values of β are included in each case for comparison.

to each window in the stable region. In order to illustrate how the different windows are weighted in the model average, in the lower panel of Fig. 13 we colour our points proportionally to their weight, calculated as in Eq. (32). Using the same colour scale, in the left (right) hand side panel Fig. 14 we depict the value of γ_* at fixed higher (lower) end of the window $a\Omega_{\max}$ as a function of the lower (higher) one. As it is visible from the example, the model average tends to prefer bigger windows with good χ_{aug}^2 , as expected. In Table V we report the values obtained for all the ensembles analyzed.

3. γ_* in the continuum limit

We have previously observed, and confirmed in the previous subsection, that for the $N_f = 1$ case, the value of γ_* is not stable as the coupling β is changed. We have sufficiently many values of β to attempt a continuum limit extrapolation. Since the mode number method described above allows computation of γ_* for individual ensembles, and there is a strong dependence of the gradient flow scale w_0/a on the fermion mass am , one might expect to be able to study dependence of the per-ensemble γ_* as a function of a/w_0 , and extrapolate to the $a/w_0 \rightarrow 0$

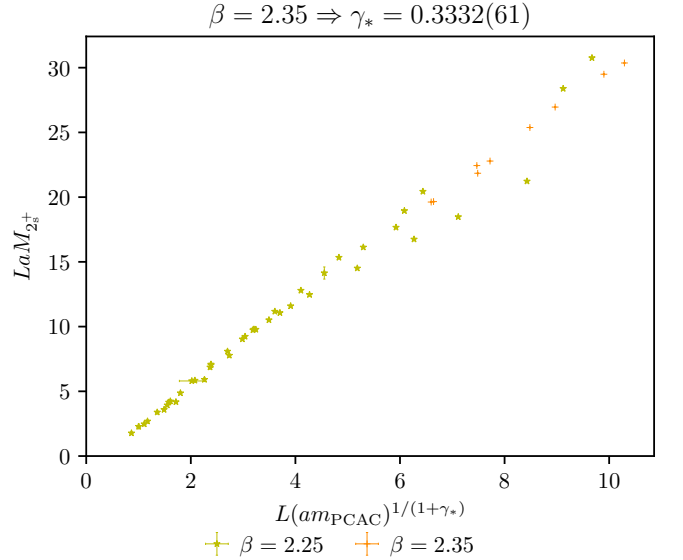


FIG. 12. Finite-volume hyperscaling fit results for $N_f = 2$, $\beta = 2.35$.

limit. However, as we show in Fig. 15, γ_* does not vary sufficiently with am to align with the trend observed as β is changed. Instead, we must use a consistently-defined scale for each β value.

We adopt, *ad hoc*, two different prescriptions for this scale and the subsequent fitting form, so that we can have some estimate of possible systematic effects. Firstly,

function. Since in our case the number of fitted parameters is the same for every window, we drop it since it corresponds to an overall factor that disappears in the normalization.

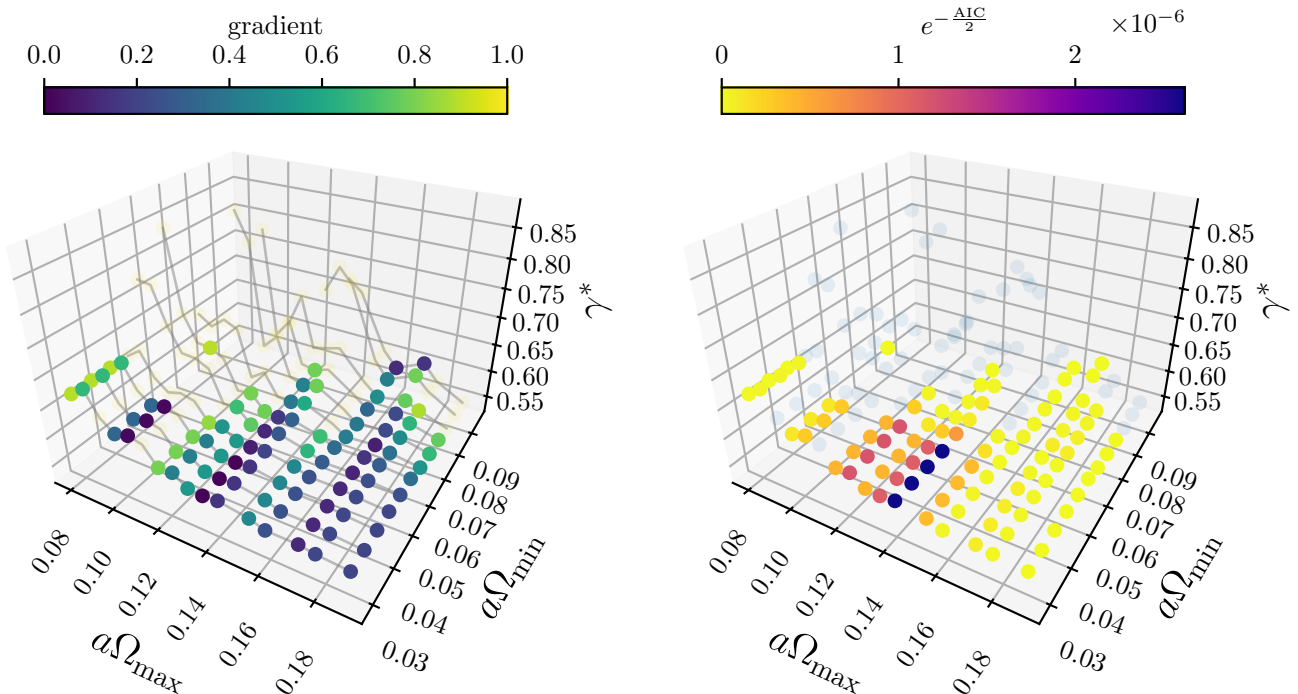


FIG. 13. Values of the anomalous dimension γ_* extracted from the fit for the ensemble DB4M11. Neighbouring points are joined by grey lines to guide the eye. *Left panel*: the colour scale of the points is proportional to the gradient, colder colour corresponds to a flatter region. All the points whose gradient is lower than a certain cutoff value are depicted with a solid marker, the others with a transparent one. *Right panel*: the colour scale of the point is proportional to the AIC weight given in Eq. (32).

we consider the behaviour of γ_* obtained from the mode number as a function of $1/\beta$ directly, shown in Fig. 16. We observe that the data begin to flatten off as β decreases. We fit these data using the *ad hoc* form

$$\gamma_*(\beta) = d_0 + d_1 e^{-d_2 \beta}, \quad (33)$$

which is inspired by assuming a linear correction in a , with the latter parameterized with an exponential in β , as suggested by the leading perturbative behaviour. This gives a continuum limit value of $\gamma_* = 0.163(24)$, with $\chi^2/\text{dof} = 12.08$. The high value of the χ^2/dof , which is mostly due to the lowest β point, suggests that we are still too far from the continuum limit for Eq. (33) to provide an accurate description of the data. It is also possible that the errors on the extracted values of γ_* are somewhat underestimated, or that an unaccounted systematic error on γ_* affects our determination. Investigating the source of this discrepancy is beyond the scope of this work. However, we remark that adding a higher order term in the exponent reduces χ^2/dof to around 7, which is still far from an acceptable value.

The second approach we consider is to take the chiral limit value for a/w_0 . This necessarily assumes that the theory is not in the conformal window, where we would expect this value to be zero; rather than infrared conformal,

here we assume that the theory is near-conformal. We extrapolate a/w_0 as a function of am_{PCAC} using a quadratic Ansatz,

$$\frac{a}{w_0} = \frac{a}{w_0^\chi} + B(am_{\text{PCAC}}) + C(am_{\text{PCAC}})^2, \quad (34)$$

where a/w_0^χ is the extrapolated chiral limit value of a/w_0 . This extrapolation is shown in Fig. 17. As β increases, a/w_0^χ approaches but does not reach zero, in agreement with our assumption of some residual global symmetry breaking. We then consider γ_* as a function of a/w_0^χ , which we plot in Fig. 18. We impose a quadratic Ansatz,

$$\gamma_*(w_0^\chi) = \gamma_*^{\text{cont.}} + c_0 \left(\frac{a}{w_0^\chi} \right) + c_1 \left(\frac{a}{w_0^\chi} \right)^2, \quad (35)$$

which gives a resulting continuum limit of $\gamma_*^{\text{cont.}} = 0.1751(65)$. As these data lie closer to the continuum limit, the uncertainty on the extrapolated value is smaller than the extrapolation in $1/\beta$ above. (There may however be systematic uncertainties not accounted for due to the choice of fit form.) The result is consistent with the limit imposed by the fit to Eq. (33). Note however that in the case discussed here the value of γ_* would be scheme dependent.

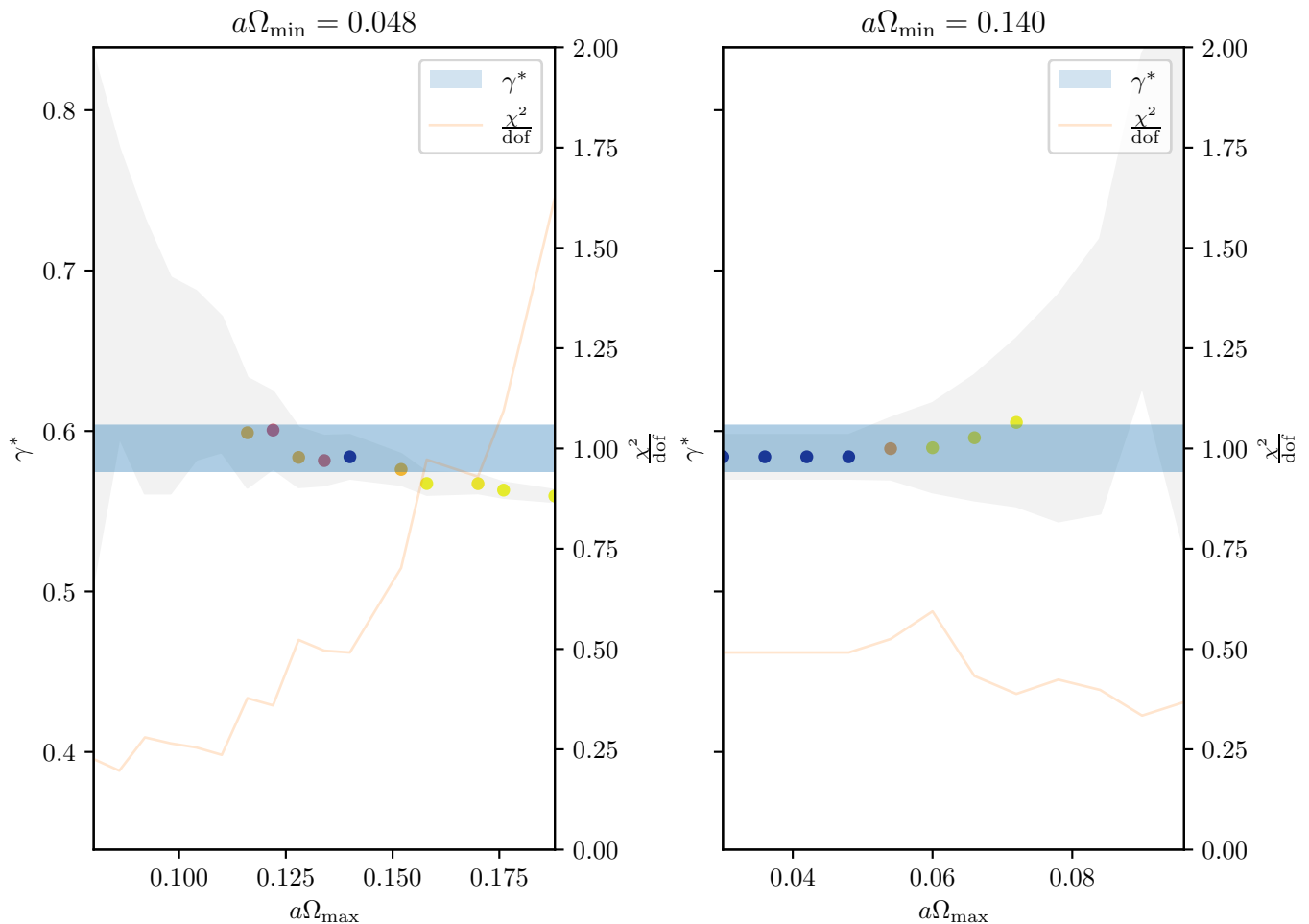


FIG. 14. Values of the anomalous dimension γ^* as a function of the higher (lower) end of the fitting window at a fixed value of lower (higher) end for the ensemble DB4M11. Error of single points are depicted as a continuous grey band, while point markers are coloured proportional to their model weight (calculated) with the same colour scale as in Fig. 14. The weighted average is represented as a horizontal blue band whose size is proportional to its statistical error. The orange solid line corresponds to the normal (i.e. not augmented) χ^2 , divided by the degrees of freedom.

Taking the mean of these two estimates, weighted by their statistical errors, gives our final estimate for the continuum limit value of the mass anomalous dimension of the $N_f = 1$ theory, $\gamma_* = 0.174(6)$.

For the $N_f = 2$ theory, we do not have data for sufficiently many values of β to perform an extrapolation; however, we observe that the values obtained in Table VI are consistent within uncertainties between the two values of β considered, suggesting they already may be close to the continuum value.

G. Comparison with chiral perturbation theory

In addition to, and to prove a contrast with, the hyperscaling case discussed above, we also probe how well a chiral perturbation theory Ansatz describes the data in the infrared limit. We fit the mass of the 2^+ scalar baryon, the pseudo-Nambu-Goldstone boson of the (po-

tentially) broken chiral symmetry, with the functional form:

$$\hat{M}_{2_s^+} = 2B\hat{m}_{\text{PCAC}}(1 + L\hat{m}_{\text{PCAC}} + D_1\hat{m}_{\text{PCAC}} \log(D_2\hat{m}_{\text{PCAC}})) \quad (36)$$

$$+ W_1 am_{\text{PCAC}} \quad (37)$$

$$+ W_2 \frac{a^2}{w_0^2}, \quad (38)$$

where hatted quantities represent the equivalent unhatted quantities normalised by the gradient flow scale w_0 . We perform a simultaneous fit across all values of β for which data is available, and then for each ensemble compute the fit value for \hat{M} given the ensemble's observed values for m_{PCAC} and w_0 .

The results for $N_f = 1$ are plotted in Fig. 19: similarly to our previous work [44], we see deviations from this form increasing as the value of am_{PCAC} decreases or the

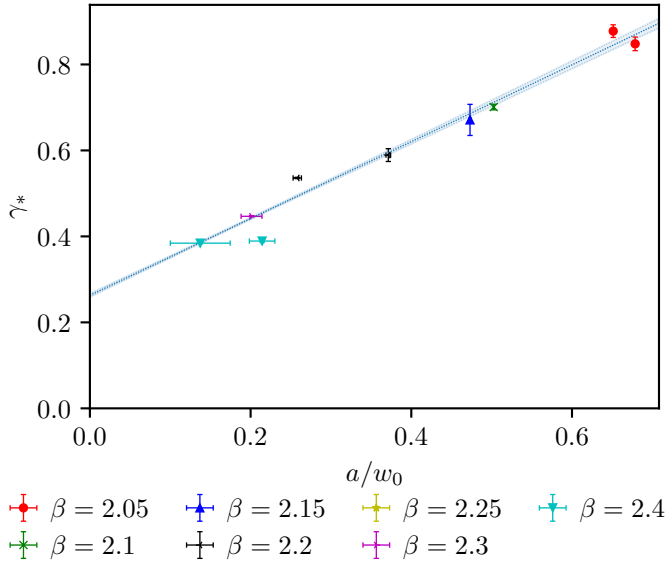


FIG. 15. The anomalous dimension γ_* obtained from the mode number plotted as a function of the per-ensemble value of the gradient flow scale a/w_0 . Included for comparison is a fit form $\gamma_*(w_0) = \gamma_*^{\text{cont.}} + c \frac{a}{w_0}$, which gives a continuum limit value $\gamma_*^{\text{cont.}} = 0.2628(35)$.

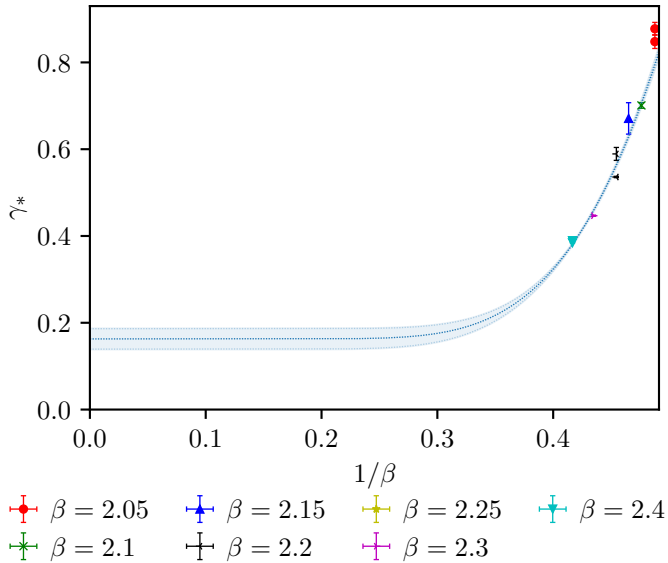


FIG. 16. The anomalous dimension γ_* obtained from the mode number plotted as a function of β . This is fitted using Eq. (33), giving a continuum limit value $\gamma_*^{\text{cont.}} = 0.163(24)$.

value of β increases. The results for $N_f = 2$, shown in Fig. 20, meanwhile, show less significant deviations. The amount that can be drawn from this is however limited, as only a single value of β is considered, and the number of degrees of freedom is reduced due to the small number of ensembles for which w_0 can be computed.

H. R ratio

In this section, we examine our recently acquired data along with older results for $SU(2)$ with $N_f = 1$ as well as with $N_f = 2$ flavors in the adjoint representation. Our aim is to explore universal characteristics that could delineate the broad parameter space of those strongly interacting gauge theories, in particular exposing their anomalous dimension as we approach the continuum.

As shown in [123], in an appropriate regime, the ratio

$$R = \frac{M_{2^{++}}}{M_{0^{++}}}, \quad (39)$$

where $M_{2^{++}}$ represents the mass of the lightest spin-2 composite state and $M_{0^{++}}$ denotes the mass of the lightest spin-0 state, has a universal behaviour that is determined by the value of the mass anomalous dimension γ_* . Therefore, the ratio R serves as a useful tool for characterizing general properties within an infrared (IR) conformal gauge theory. Several noteworthy characteristics render the observable R particularly significant. Crucially, R exhibits scheme-independence, and remains unaffected by the internal global symmetries of the theory. Hence, the comparison of R values computed in theories featuring vastly different internal symmetries and symmetry-breaking patterns provides an additional approach to the determination of γ_* that proves especially valuable for gauge theories incorporating fermionic fields, where the intricacies of chiral symmetry and its breaking introduce non-trivial, model-dependent features.

Prior to presenting numerical results for R , let's briefly outline the anticipated behavior of a conformal theory under deformation by a fermion mass m . For a small, finite deforming mass region, spectral masses are expected to scale as $M \propto m^{1/\Delta}$ where $\Delta = 1 + \gamma_*$ represents the scaling dimension. Since a finite lattice volume imposes an absolute infrared cutoff, an appropriate scaling variable to consider on a finite box with typical dimension L is $x = Lm^{1/\Delta}$. Consequently, the mass of a generic i^{th} state acquires a dependence on x , which can be expressed as $LM_i = f_i(x)$, with f_i an *a priori* unknown function. At leading order in x , for a state with mass M_0 , this yields $LM_0 \propto x$, and through back substitution, $LM_i = f_i(LM_0)$. Consequently, when considering mass ratios, the explicit dependence on the lattice extent cancels out, enabling comparison of data across different volumes:

$$\frac{M_i}{M_j} = \frac{f_i(LM_0)}{f_j(LM_0)}. \quad (40)$$

We anticipate that the behavior of R will exhibit four distinct regimes. For large values of m , R tends to align closely with the value observed in pure $SU(2)$ Yang-Mills theory, determined in lattice studies as $R = 1.44(4)$ [109, 124]. Conversely, at small m , the regime that is realised will hinge on the lattice size L . In sufficiently large volumes, the observed physics displays con-

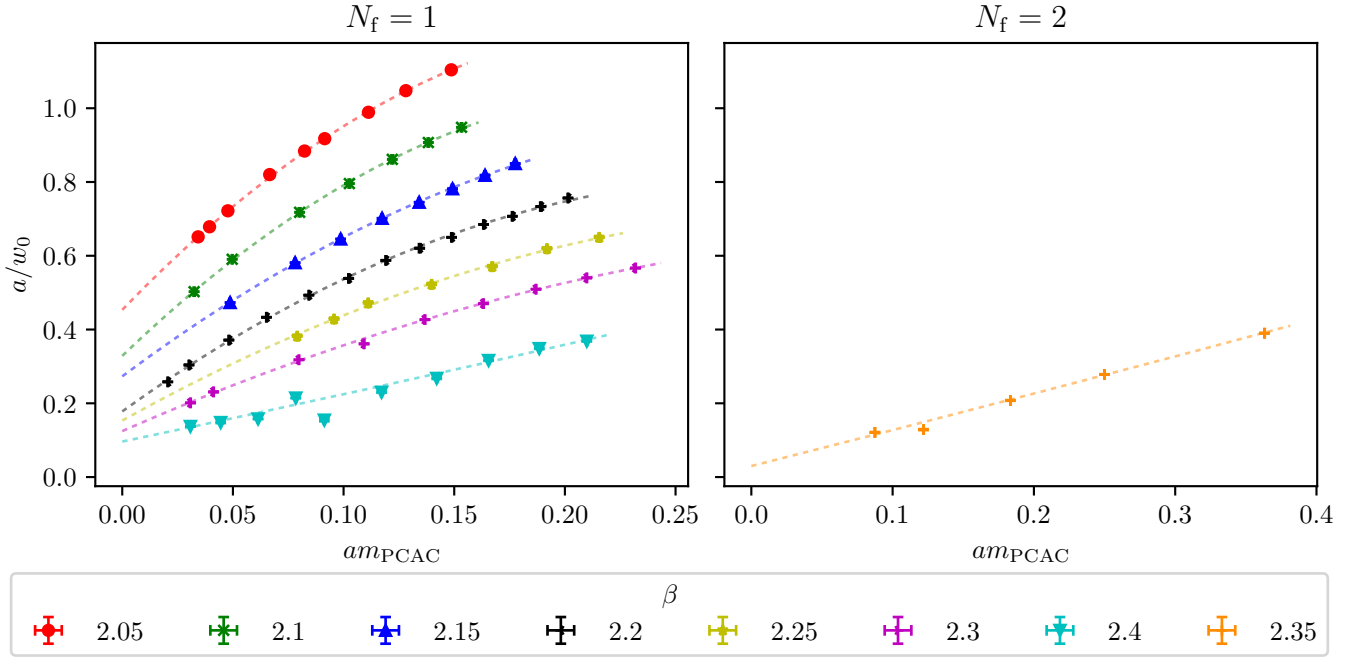


FIG. 17. The reciprocal gradient flow scale a/w_0 plotted as a function of am_{PCAC} for both $N_f = 1$ (left) and 2 (right), including fits to Eq. (34) for each β value.

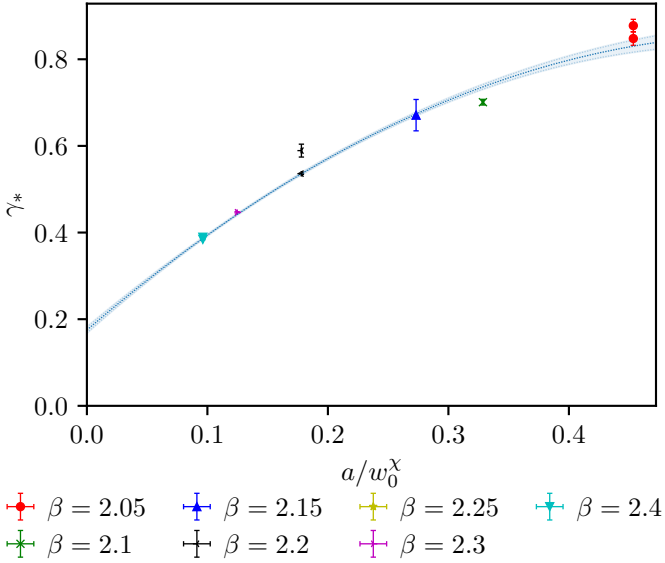


FIG. 18. The anomalous dimension γ_* obtained from the mode number plotted as a function of the chiral limit reciprocal gradient flow scale a/w_0^χ . This is fitted using Eq. (35), giving a continuum limit value $\gamma_*^{\text{cont.}} = 0.1751(65)$.

fining properties due to the mass deformation. Conversely, at very small volumes, the theory transitions to the so-called “femto-universe” regime [123], where previous studies suggest R approaches unity [125–127]. However, for L large enough and m small enough, an intermediate regime of R exists where conformal behavior can

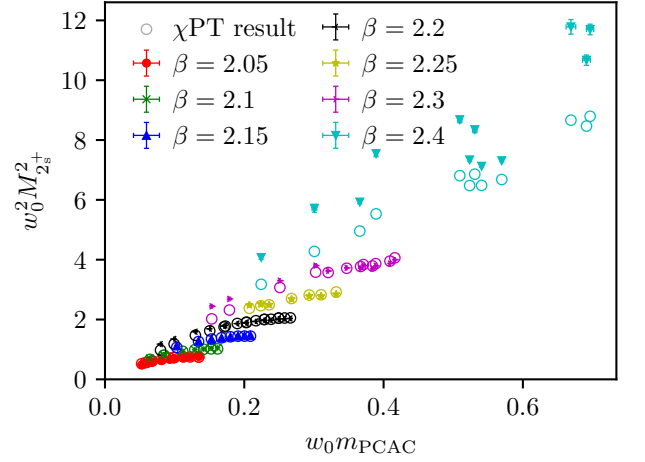


FIG. 19. Comparison of the mass observed for the 2^+ for the $N_f = 1$ theory (error bars) with a fit of these data to a chiral perturbation theory Ansatz (open circles).

be observed. This intermediate region is of particular interest as in it R can be extrapolated to obtain a chiral limit value that provides a universal signature of conformal behaviour. Note that whether the intermediate region is observed in a given simulation is a consequence of the choice of the lattice parameters, since a same value of x can be obtained by tuning m and L to very different regimes.

Given the universal behaviour of R , to gain insights on the anomalous dimension, we opt to contrast our findings

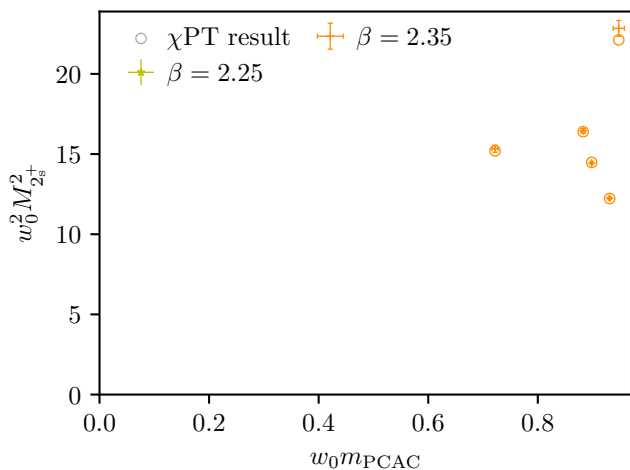


FIG. 20. Comparison of the mass observed for the 2^+ for the $N_f = 2$ theory (error bars) with a fit of these data to a chiral perturbation theory Ansatz (open circles).

with a toy model constructed using principles of gauge-gravity duality [123]. This calculable model, developed within the bottom-up approach to holography, incorporates only an operator with a scaling dimension Δ deforming the theory. Leveraging the obtained results for the anomalous dimension, we can compare the measured ratio with expectations derived from the toy model utilizing the corresponding value of Δ . Further elucidation on this concept is available in Ref. [123].

In Fig. 21, we display our findings regarding R across seven distinct values of the coupling β for $SU(2)$ at $N_f = 1$. The data for the initial four plots have been previously showcased in Ref. [44]. Our results are juxtaposed with the R ratio for the pure $SU(2)$ Yang-Mills theory (depicted by the blue dashed line) and with predictions derived from the gauge-gravity inspired toy model (shown as the upper band). It is worthy to note that the conformal prediction varies for each value of β due to differing measured values of γ_* . Additionally, for $\beta = 2.05$, the width of the band differs slightly from that presented in Ref. [123] due to a different method of extracting γ_* resulting in a more conservative estimation of the error: in Ref. [123], the results were derived using the Dirac mode number; in contrast, our current investigation employs the finite-size hyperscaling Ansatz.

For large values of LM_{0++} , the data for $\beta = 2.05$ up to $\beta = 2.3$ tends toward the pure gauge prediction, in line with expectations. As LM_{0++} decreases, approaching the smallest values of β , the calculations become consistent with the conformal plateau, particularly for larger R . At $\beta = 2.1$ and, to a lesser extent, $\beta = 2.15$, there is some indication of behavior diverging from confinement, although the ratio does not rise sufficiently to match the value predicted by the gauge/gravity model. Notably, for the highest values of β , the results for R do not significantly exceed the Yang-Mills value, even for large LM_{0++} , possibly indicating an increasing difficulty in re-

alising the regime that is relevant for near-conformality in this observable as β increases. Interestingly, at the highest two values of β and lower LM_{0++} , there is clear evidence of R decreasing towards $R \approx 1$, indicating a femto-universe behavior; In this region, the mass of the ground scalar glueball as well as the tensor glueball become approximately degenerate due to the lattice box geometry.

Overall we observe that for $N_f = 1$, the value of R decreases from a scenario with a large anomalous dimension ($R \gg 1$) as the value of β increases and approaches the continuum limit. In fact, any signals of conformality become weaker and are eventually lost, which aligns with the idea that as the continuum is approached, the anomalous dimension decreases. This effect increases the difficulty in tuning the simulation to the intermediate region that is relevant for determining the anomalous dimension using the universality of R . Followingly, for large values of LM_{0++} , the ratio R converges to the pure Yang-Mills prediction of $R = 1.44(4)$, enhancing the scenario of existing universality. Finally, for small values of LM_{0++} the R -ratio appears to be aligned with the femto-universe scenario.

Similarly, in Fig. 22, we present our results for the ratio M_{2++}/M_{0++} at inverse couplings of $\beta = 2.25$ and $\beta = 2.35$. The findings for $\beta = 2.25$ were previously discussed in detail in Ref. [123]. Our current study extends these earlier results by including data for $\beta = 2.35$, attempting for a more comprehensive analysis of the behavior of this mass ratio under varying coupling conditions.

In general, the results for the case of $N_f = 2$ exhibit a significantly higher degree of scatter, making it difficult to draw clear and robust conclusions. This behavior is illustrated by a large number of data points aligning with the $SU(2)$ pure gauge prediction, while many other points lie significantly lower, approaching unity. We consider these latter data points to be affected by significant finite volume effects, which aligns with the femto-universe hypothesis.

Bearing the above in mind, let us attempt to understand our numerical findings. First, for large values of LM_{0++} , the data for β of 2.25 tends to align with the pure gauge prediction, as expected. As LM_{0++} decreases, the calculations become consistent with the conformal plateau prediction; it appears that the latter is realised for values of R ranging for $LM_{0++} = 8 - 10$. This feature appears to weaken as we move closer to the continuum. Namely, for $\beta = 2.35$ we cannot see an agreement with the conformal model anymore at intermediate values of LM_{0++} apart from one data-point for the very low values of LM_{0++} which appears to be an outlier. Instead, we observe that most of the data points are surrounding the pure gauge theory prediction. This suggests once more that the anomalous dimension weakens as we approach the continuum limit.

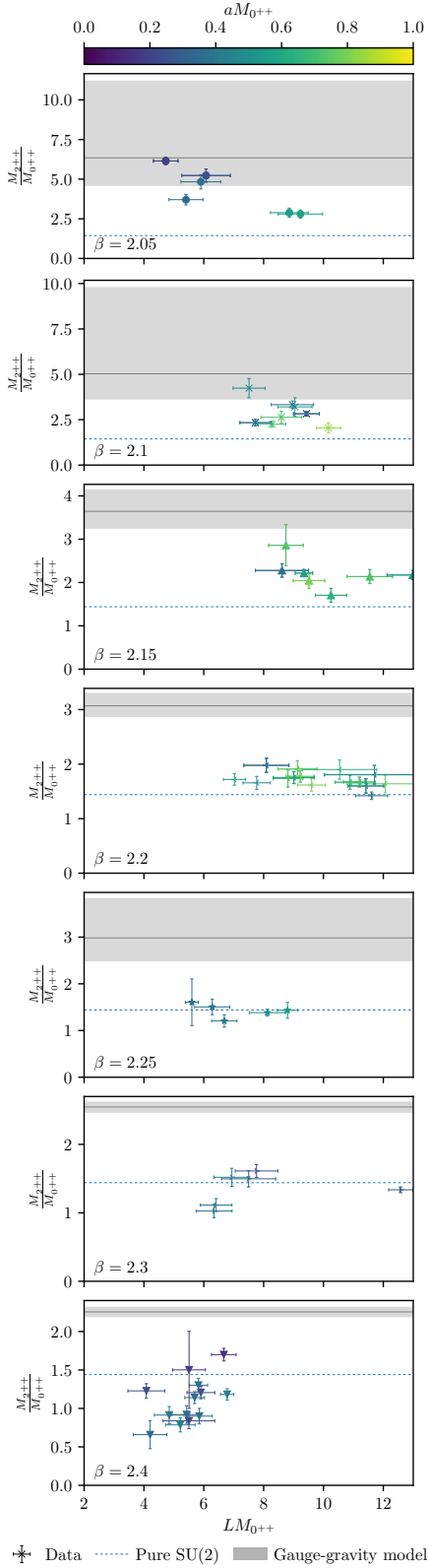


FIG. 21. The value of the R ratio observed for $N_f = 1$ for each value of β .

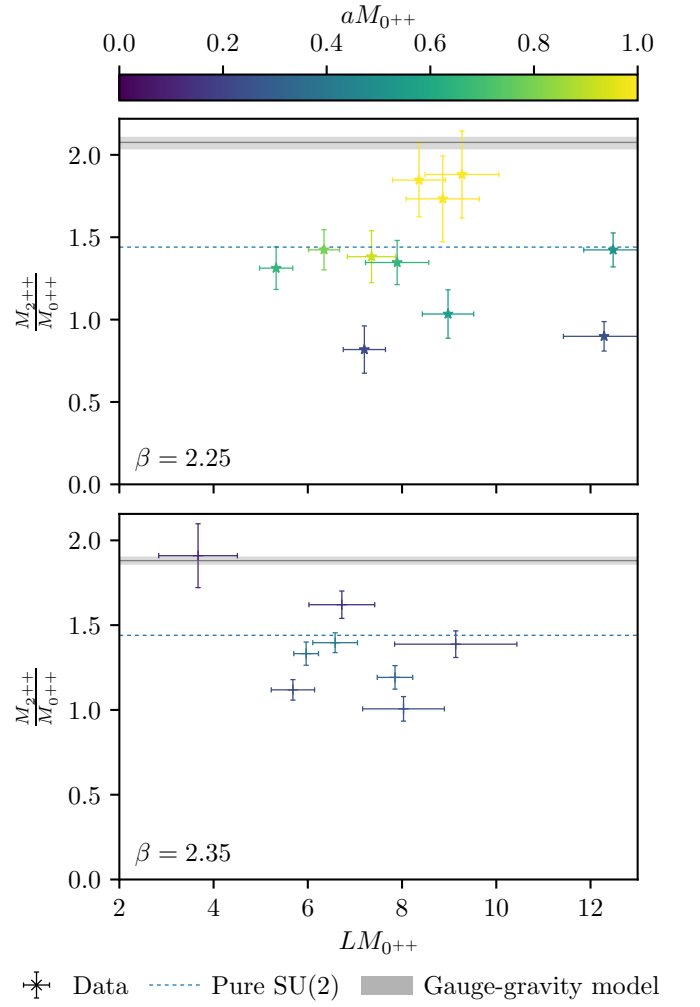


FIG. 22. The value of the R ratio observed for $N_f = 2$, $\beta = 2.35$.

IV. CONCLUSIONS

Armed with the purpose of advancing the characterisation of the infrared behaviour of $SU(2)$ gauge theories with $N_f = 1$ and $N_f = 2$ Dirac fermion flavours transforming in the adjoint representation, we have performed an extended study of the former model in bare parameter space, with the intent of extrapolating the results to the continuum limit. For the considered values of the parameters, we have provided a detailed study of the mass spectrum, which has enabled us to extract the fermion condensate anomalous dimension using the expected hyperscaling behaviour for (near-)conformal systems. In addition, the anomalous dimension has been investigated making use of a mode number analysis of the Dirac spectrum and of the universal behaviour of the ratio of the mass of the lightest spin-two particle over the mass of the scalar. With different efficacy, all methods give consistent results and point towards heavy corrections to the anomalous dimension as the continuum

limit is approached. Using *ad hoc* Ansätze, we have extrapolated the anomalous dimension to zero lattice spacing. Neglecting the systematics, including the one coming from the extrapolation, which can be somewhat large, our final result for the $N_f = 1$ theory is $\gamma_* = 0.174(6)$. In contrast with earlier findings at larger lattice spacings, this value is significantly smaller than one. Barring very large lattice artefacts, a scenario that would need to be investigated further, the strong dependence of the anomalous dimension on the lattice spacing seems to exclude a clear signature of infrared conformality. We have also performed a chiral perturbation theory analysis, which shows that a regime with detectable chiral symmetry breaking is also excluded. This however does not exclude the possibility that the infrared dynamics of the model will result in a small breaking of chiral symmetry. Putting together both the near-conformal and the chiral perturbation theory analysis, the most likely conclusion is that the theory is in the chiral symmetry broken phase, but rather close to the sill of conformality.

Our calculations for the $N_f = 2$ theory are more limited in scope, as we have only two lattice spacing values available, one from an earlier study and one investigated explicitly in this work. Combining the corresponding data with an analysis that parallels the $N_f = 1$ case, within the limitations of the information that can be extracted, we note a milder dependence of γ_* on the lattice spacing and again albeit milder an intrinsic difficulty of chiral perturbation theory to describe the results. A likely conclusion is that the $N_f = 2$ model lies inside the conformal window, and has a small anomalous dimension.

After over 15 years of chasing the infrared behaviour of those models, this very important quest appears to be far from over. However, our work has pushed the boundaries of what can be done with state of the art resources using a few millions hours of A100 GPUs with the formulation of the action adopted so far. Future investigations call for the use of actions that have smaller lattice spacing corrections, and can hence produce more physical results at a relatively coarse lattice spacing, and are more amenable to be pushed towards the chiral limit. To carry on this line of investigation, the possibilities that we are currently exploring include Möbius domain wall fermions (see, e.g., [128]) and Pauli-Villars bosons [129].

ACKNOWLEDGMENTS

A.A. was supported by the Horizon 2020 European research infrastructures programme “NI4OS-Europe” with

grant agreement no. 85764, by “SimEA” project funded by the European Union’s Horizon 2020 research and innovation programme under grant agreement No 810660, as well as by the “EuroCC” project funded by the “Deputy Ministry of Research, Innovation and Digital Policy and the Cyprus Research and Innovation Foundation” as well as by the European High-Performance Computing Joint Undertaking (JU) under grant agreement No. 101101903.

P.B. acknowledges support by the project H2020-MSCAITN-2018- 813942 (EuroPLEx) and the EU Horizon 2020 research and innovation programme and by the Grant DGA-FSE grant 2020-E21-17R Aragon Government and the European Union - NextGenerationEU Recovery and Resilience Program on “Astrofísica y Física de Altas Energías” CEFCA-CAPA-ITAINNOVA.

The work of E.B. and J.L. has been supported by the UKRI Science and Technology Facilities Council (STFC) Research Software Engineering Fellowship EP/V052489/1. The work of E.B., J.L., and B.L. has been supported in part by the EPSRC ExCALIBUR programme ExaTEPP (project EP/X017168/1). E.B. and B.L. have been partly supported by the STFC Consolidated Grant No. ST/T000813/1. B.L. received funding from the European Research Council (ERC) under the European Union’s Horizon 2020 research and innovation program under Grant Agreement No. 813942.

G.B. is funded by the Deutsche Forschungsgemeinschaft (DFG) under Grant No. 432299911 and 431842497.

This work used the DiRAC Extreme Scaling service Tursa at the University of Edinburgh, managed by the Edinburgh Parallel Computing Centre on behalf of the STFC DiRAC HPC Facility (www.dirac.ac.uk). The DiRAC service at Edinburgh was funded by BEIS, UKRI and STFC capital funding and STFC operations grants. DiRAC is part of the UKRI Digital Research Infrastructure. We acknowledge the support of the Supercomputing Wales project, which is part-funded by the European Regional Development Fund (ERDF) via Welsh Government.

Open access statement For the purpose of open access, the authors have applied a Creative Commons Attribution (CC BY) licence to any Author Accepted Manuscript version arising.

Research Data Access Statement The data generated for this manuscript can be downloaded from Ref.[102], in addition to data from previous work already available from Ref. [130] and the analysis code from Ref. [131].

-
- [1] S. Weinberg, Phys. Rev. D **13**, 974 (1976), [Addendum: Phys.Rev.D 19, 1277–1280 (1979)].
 - [2] L. Susskind, Phys. Rev. D **20**, 2619 (1979).
 - [3] E. Eichten and K. D. Lane, Phys. Lett. B **90**, 125 (1980).
 - [4] B. Holdom, Phys. Rev. D **24**, 1441 (1981).
 - [5] B. Holdom, Phys. Lett. B **150**, 301 (1985).
 - [6] K. Yamawaki, M. Bando, and K.-i. Matumoto, Phys. Rev. Lett. **56**, 1335 (1986).
 - [7] T. W. Appelquist, D. Karabali, and L. C. R. Wijewardhana, Phys. Rev. Lett. **57**, 957 (1986).

- [8] D. B. Kaplan and H. Georgi, *Phys. Lett. B* **136**, 183 (1984).
- [9] H. Georgi, *Phys. Lett. B* **151**, 57 (1985).
- [10] M. J. Dugan, H. Georgi, and D. B. Kaplan, *Nucl. Phys. B* **254**, 299 (1985).
- [11] J. Barnard, T. Gherghetta, and T. S. Ray, *JHEP* **02**, 002, arXiv:1311.6562 [hep-ph].
- [12] G. Ferretti and D. Karateev, *JHEP* **03**, 077, arXiv:1312.5330 [hep-ph].
- [13] G. Ferretti, *JHEP* **06**, 107, arXiv:1604.06467 [hep-ph].
- [14] G. Cacciapaglia, G. Ferretti, T. Flacke, and H. Serôdio, *Front. in Phys.* **7**, 22 (2019), arXiv:1902.06890 [hep-ph].
- [15] F. Sannino and M. Shifman, *Phys. Rev. D* **69**, 125004 (2004), arXiv:hep-th/0309252.
- [16] F. Sannino and K. Tuominen, *Phys. Rev. D* **71**, 051901 (2005), arXiv:hep-ph/0405209.
- [17] D. D. Dietrich, F. Sannino, and K. Tuominen, *Phys. Rev. D* **72**, 055001 (2005), arXiv:hep-ph/0505059.
- [18] D. D. Dietrich and F. Sannino, *Phys. Rev. D* **75**, 085018 (2007), arXiv:hep-ph/0611341.
- [19] N. Evans and K. S. Rigatos, *Phys. Rev. D* **103**, 094022 (2021), arXiv:2012.00032 [hep-ph].
- [20] J.-W. Lee, *Phys. Rev. D* **103**, 076006 (2021), arXiv:2008.12223 [hep-ph].
- [21] G. Aad *et al.* (ATLAS), *Phys. Lett. B* **716**, 1 (2012), arXiv:1207.7214 [hep-ex].
- [22] S. Chatrchyan *et al.* (CMS), *Phys. Lett. B* **716**, 30 (2012), arXiv:1207.7235 [hep-ex].
- [23] L. Del Debbio, B. Lucini, A. Patella, C. Pica, and A. Rago, *Phys. Rev. D* **80**, 074507 (2009), arXiv:0907.3896 [hep-lat].
- [24] A. J. Hietanen, K. Rummukainen, and K. Tuominen, *Phys. Rev. D* **80**, 094504 (2009), arXiv:0904.0864 [hep-lat].
- [25] Z. Fodor, K. Holland, J. Kuti, D. Negradi, and C. Schroeder, *Phys. Lett. B* **681**, 353 (2009), arXiv:0907.4562 [hep-lat].
- [26] F. Bursa, L. Del Debbio, L. Keegan, C. Pica, and T. Pickup, *Phys. Rev. D* **81**, 014505 (2010), arXiv:0910.4535 [hep-ph].
- [27] L. Del Debbio, B. Lucini, A. Patella, C. Pica, and A. Rago, *Phys. Rev. D* **82**, 014509 (2010), arXiv:1004.3197 [hep-lat].
- [28] L. Del Debbio, B. Lucini, A. Patella, C. Pica, and A. Rago, *Phys. Rev. D* **82**, 014510 (2010), arXiv:1004.3206 [hep-lat].
- [29] Z. Fodor, K. Holland, J. Kuti, D. Negradi, C. Schroeder, K. Holland, J. Kuti, D. Negradi, and C. Schroeder, *Phys. Lett. B* **703**, 348 (2011), arXiv:1104.3124 [hep-lat].
- [30] F. Bursa, L. Del Debbio, D. Henty, E. Kerrane, B. Lucini, A. Patella, C. Pica, T. Pickup, and A. Rago, *Phys. Rev. D* **84**, 034506 (2011), arXiv:1104.4301 [hep-lat].
- [31] S. Catterall, L. Del Debbio, J. Giedt, and L. Keegan, *Phys. Rev. D* **85**, 094501 (2012), arXiv:1108.3794 [hep-ph].
- [32] T. DeGrand, Y. Shamir, and B. Svetitsky, *Phys. Rev. D* **83**, 074507 (2011), arXiv:1102.2843 [hep-lat].
- [33] S. Catterall and F. Sannino, *Phys. Rev. D* **76**, 034504 (2007), arXiv:0705.1664 [hep-lat].
- [34] L. Del Debbio, A. Patella, and C. Pica, *Phys. Rev. D* **81**, 094503 (2010), arXiv:0805.2058 [hep-lat].
- [35] A. J. Hietanen, J. Rantaharju, K. Rummukainen, and K. Tuominen, *JHEP* **05**, 025, arXiv:0812.1467 [hep-lat].
- [36] S. Catterall, J. Giedt, F. Sannino, and J. Schneible, *JHEP* **11**, 009, arXiv:0807.0792 [hep-lat].
- [37] L. Del Debbio, B. Lucini, C. Pica, A. Patella, A. Rago, and S. Roman, in *31st International Symposium on Lattice Field Theory* (2013) arXiv:1311.5597 [hep-lat].
- [38] A. Hasenfratz, D. Schaich, and A. Veernala, *JHEP* **06**, 143, arXiv:1410.5886 [hep-lat].
- [39] A. Athenodorou, E. Bennett, G. Bergner, and B. Lucini, *Phys. Rev. D* **91**, 114508 (2015), arXiv:1412.5994 [hep-lat].
- [40] T. Appelquist *et al.*, *Phys. Rev. D* **93**, 114514 (2016), arXiv:1601.04027 [hep-lat].
- [41] A. Hasenfratz and D. Schaich, *JHEP* **02**, 132, arXiv:1610.10004 [hep-lat].
- [42] G. Bergner, P. Giudice, I. Montvay, G. Münster, and S. Piemonte, *Phys. Rev. D* **96**, 034504 (2017), arXiv:1610.01576 [hep-lat].
- [43] G. Bergner, P. Giudice, G. Münster, P. Scior, I. Montvay, and S. Piemonte, *JHEP* **01**, 119, arXiv:1712.04692 [hep-lat].
- [44] A. Athenodorou, E. Bennett, G. Bergner, and B. Lucini, *Phys. Rev. D* **104**, 074519 (2021), arXiv:2103.10485 [hep-lat].
- [45] T. DeGrand, Y. Shamir, and B. Svetitsky, *Phys. Rev. D* **85**, 074506 (2012), arXiv:1202.2675 [hep-lat].
- [46] T. DeGrand, Y. Shamir, and B. Svetitsky, *Phys. Rev. D* **88**, 054505 (2013), arXiv:1307.2425 [hep-lat].
- [47] T. DeGrand, Y. Liu, E. T. Neil, Y. Shamir, and B. Svetitsky, *Phys. Rev. D* **91**, 114502 (2015), arXiv:1501.05665 [hep-lat].
- [48] T. DeGrand and Y. Shamir, *Phys. Rev. D* **92**, 075039 (2015), arXiv:1508.02581 [hep-ph].
- [49] T. DeGrand, M. Golterman, E. T. Neil, and Y. Shamir, *Phys. Rev. D* **94**, 025020 (2016), arXiv:1605.07738 [hep-ph].
- [50] T. A. DeGrand, M. Golterman, W. I. Jay, E. T. Neil, Y. Shamir, and B. Svetitsky, *Phys. Rev. D* **94**, 054501 (2016), arXiv:1606.02695 [hep-lat].
- [51] V. Ayyar, T. DeGrand, M. Golterman, D. C. Hackett, W. I. Jay, E. T. Neil, Y. Shamir, and B. Svetitsky, *Phys. Rev. D* **97**, 074505 (2018), arXiv:1710.00806 [hep-lat].
- [52] E. Bennett, D. K. Hong, J.-W. Lee, C. J. D. Lin, B. Lucini, M. Piai, and D. Vadacchino, *JHEP* **03**, 185, arXiv:1712.04220 [hep-lat].
- [53] V. Ayyar, T. DeGrand, D. C. Hackett, W. I. Jay, E. T. Neil, Y. Shamir, and B. Svetitsky, *Phys. Rev. D* **97**, 114505 (2018), arXiv:1801.05809 [hep-ph].
- [54] V. Ayyar, T. DeGrand, D. C. Hackett, W. I. Jay, E. T. Neil, Y. Shamir, and B. Svetitsky, *Phys. Rev. D* **97**, 114502 (2018), arXiv:1802.09644 [hep-lat].
- [55] V. Ayyar, T. DeGrand, D. C. Hackett, W. I. Jay, E. T. Neil, Y. Shamir, and B. Svetitsky, *Phys. Rev. D* **99**, 094502 (2019), arXiv:1812.02727 [hep-ph].
- [56] E. Bennett, D. K. Hong, J.-W. Lee, C. J. D. Lin, B. Lucini, M. Piai, and D. Vadacchino, *JHEP* **12**, 053, arXiv:1909.12662 [hep-lat].
- [57] E. Bennett, D. K. Hong, J.-W. Lee, C.-J. D. Lin, B. Lucini, M. Mesiti, M. Piai, J. Rantaharju, and D. Vadacchino, *Phys. Rev. D* **101**, 074516 (2020), arXiv:1912.06505 [hep-lat].
- [58] G. Cossu, L. Del Debbio, M. Panero, and D. Preti, *Eur. Phys. J. C* **79**, 638 (2019), arXiv:1904.08885 [hep-lat].
- [59] E. Bennett, D. K. Hong, H. Hsiao, J.-W. Lee, C. J. D. Lin, B. Lucini, M. Mesiti, M. Piai, and D. Vadacchino,

- Phys. Rev. D **106**, 014501 (2022), arXiv:2202.05516 [hep-lat].
- [60] L. Del Debbio, A. Lupo, M. Panero, and N. Tantalo, Eur. Phys. J. C **83**, 220 (2023), arXiv:2211.09581 [hep-lat].
- [61] E. Bennett, J. Holligan, D. K. Hong, H. Hsiao, J.-W. Lee, C. J. D. Lin, B. Lucini, M. Mesiti, M. Piai, and D. Vadacchino, Universe **9**, 236 (2023), arXiv:2304.01070 [hep-lat].
- [62] E. Bennett *et al.*, Phys. Rev. D **108**, 094508 (2023), arXiv:2306.11649 [hep-lat].
- [63] A. Maas and F. Zierler, PoS **LATTICE2021**, 130 (2022), arXiv:2109.14377 [hep-lat].
- [64] F. Zierler and A. Maas, PoS **LHCP2021**, 162 (2021).
- [65] S. Kulkarni, A. Maas, S. Mee, M. Nikolic, J. Pradler, and F. Zierler, SciPost Phys. **14**, 044 (2023), arXiv:2202.05191 [hep-ph].
- [66] B. Lucini, Phil. Trans. Roy. Soc. Lond. A **368**, 3657 (2010), arXiv:0911.0020 [hep-ph].
- [67] L. Del Debbio and R. Zwicky, Phys. Rev. D **82**, 014502 (2010), arXiv:1005.2371 [hep-ph].
- [68] T. Appelquist, J. Ingoldby, and M. Piai, JHEP **07**, 035, arXiv:1702.04410 [hep-ph].
- [69] T. Appelquist, J. Ingoldby, and M. Piai, Phys. Rev. D **101**, 075025 (2020), arXiv:1908.00895 [hep-ph].
- [70] A. Patella, Phys. Rev. D **86**, 025006 (2012), arXiv:1204.4432 [hep-lat].
- [71] Z. Fodor, K. Holland, J. Kuti, D. Negradi, and C. H. Wong, JHEP **11**, 007, arXiv:1208.1051 [hep-lat].
- [72] M. García Pérez, A. González-Arroyo, L. Keegan, and M. Okawa, JHEP **08**, 034, arXiv:1506.06536 [hep-lat].
- [73] C. Pica, PoS **LATTICE2016**, 015 (2016), arXiv:1701.07782 [hep-lat].
- [74] O. Witzel, PoS **LATTICE2018**, 006 (2019), arXiv:1901.08216 [hep-lat].
- [75] M. García Pérez, PoS **LATTICE2019**, 276 (2020), arXiv:2001.10859 [hep-lat].
- [76] T. Appelquist, J. Ingoldby, and M. Piai, Universe **9**, 10 (2023), arXiv:2209.14867 [hep-ph].
- [77] K. Rummukainen and K. Tuominen, Universe **8**, 188 (2022).
- [78] J.-W. Lee (2024) arXiv:2402.01087 [hep-lat].
- [79] W. E. Caswell, Phys. Rev. Lett. **33**, 244 (1974).
- [80] T. Banks and A. Zaks, Nucl. Phys. B **196**, 189 (1982).
- [81] N. Seiberg, Nucl. Phys. B **435**, 129 (1995), arXiv:hep-th/9411149.
- [82] M. Unsal, Phys. Rev. D **80**, 065001 (2009), arXiv:0709.3269 [hep-th].
- [83] G. Basar, A. Cherman, D. Dorigoni, and M. Ünsal, Phys. Rev. Lett. **111**, 121601 (2013), arXiv:1306.2960 [hep-th].
- [84] M. M. Anber and E. Poppitz, Phys. Rev. D **98**, 034026 (2018), arXiv:1805.12290 [hep-th].
- [85] Z. Bi and T. Senthil, Phys. Rev. X **9**, 021034 (2019), arXiv:1808.07465 [cond-mat.str-el].
- [86] C. Córdova and T. T. Dumitrescu, (2018), arXiv:1806.09592 [hep-th].
- [87] Z. Wan and J. Wang, Phys. Rev. D **99**, 065013 (2019), arXiv:1812.11955 [hep-th].
- [88] E. Poppitz and T. A. Ryttov, Phys. Rev. D **100**, 091901 (2019), arXiv:1904.11640 [hep-th].
- [89] Z. Bi, A. Grebe, G. Kanwar, P. Ledwith, D. Murphy, and M. L. Wagman, PoS **LATTICE2019**, 127 (2019), arXiv:1912.11723 [hep-lat].
- [90] G. Bergner, J. C. Lopez, S. Piemonte, and I. S. Calero, Phys. Rev. D **106**, 094507 (2022), arXiv:2205.00792 [hep-lat].
- [91] G. Bergner and S. Piemonte, Phys. Rev. D **103**, 014503 (2021), [Erratum: Phys.Rev.D 107, 019902 (2023)], arXiv:2008.02855 [hep-lat].
- [92] T. A. Ryttov and F. Sannino, Phys. Rev. D **78**, 115010 (2008), arXiv:0809.0713 [hep-ph].
- [93] E. Bennett, A. Athenodorou, G. Bergner, P. Butti, and B. Lucini, PoS **LATTICE2022**, 204 (2023), arXiv:2212.09173 [hep-lat].
- [94] S. Duane, A. D. Kennedy, B. J. Pendleton, and D. Roweth, Phys. Lett. B **195**, 216 (1987).
- [95] A. D. Kennedy, I. Horvath, and S. Sint, Nucl. Phys. B Proc. Suppl. **73**, 834 (1999), arXiv:hep-lat/9809092.
- [96] C. Pica and HiRep contributors, HiRep, <https://github.com/claudiopica/HiRep>.
- [97] A. Yamaguchi, P. Boyle, G. Cossu, G. Filaci, C. Lehner, and A. Portelli, PoS **LATTICE2021**, 035 (2022), arXiv:2203.06777 [hep-lat].
- [98] P. Boyle and Grid contributors, Grid, <https://github.com/paboyle/Grid>.
- [99] M. Luscher, Commun. Math. Phys. **85**, 39 (1982).
- [100] C. Alexandrou, A. Athenodorou, K. Cichy, A. Dromard, E. Garcia-Ramos, K. Jansen, U. Wenger, and F. Zimmermann, Eur. Phys. J. C **80**, 424 (2020), arXiv:1708.00696 [hep-lat].
- [101] M. Lüscher, JHEP **08**, 071, [Erratum: JHEP 03, 092 (2014)], arXiv:1006.4518 [hep-lat].
- [102] A. Athenodorou, E. Bennett, G. Bergner, J. Lenz, and B. Lucini, SU(2) gauge theory with one and two adjoint fermions towards the continuum limit — data release, doi:10.5281/zenodo.13128505 (2024).
- [103] E. Bennett and B. Lucini, Eur. Phys. J. C **73**, 2426 (2013), arXiv:1209.5579 [hep-lat].
- [104] S. Borsányi, S. Dürr, Z. Fodor, C. Hoelbling, S. D. Katz, S. Krieg, T. Kurth, L. Lellouch, T. Lippert, and C. McNeile (BMW), JHEP **09**, 010, arXiv:1203.4469 [hep-lat].
- [105] A. Athenodorou and M. Teper, JHEP **11**, 172, arXiv:2007.06422 [hep-lat].
- [106] M. Luscher and P. Weisz, Nucl. Phys. B **240**, 349 (1984).
- [107] M. Luscher and U. Wolff, Nucl. Phys. B **339**, 222 (1990).
- [108] B. Berg and A. Billoire, Nucl. Phys. B **221**, 109 (1983).
- [109] B. Lucini, M. Teper, and U. Wenger, JHEP **06**, 012, arXiv:hep-lat/0404008.
- [110] M. Teper, Phys. Lett. B **183**, 345 (1987).
- [111] A. Athenodorou, B. Bringoltz, and M. Teper, JHEP **02**, 030, arXiv:1007.4720 [hep-lat].
- [112] P. Goddard, J. Goldstone, C. Rebbi, and C. Thorn, Nuclear Physics B **56**, 109 (1973).
- [113] L. Del Debbio, B. Lucini, A. Patella, and C. Pica, JHEP **03**, 062, arXiv:0712.3036 [hep-th].
- [114] F. Joswig, S. Kuberski, J. T. Kuhlmann, and J. Neuenendorf, Comput. Phys. Commun. **288**, 108750 (2023), arXiv:2209.14371 [hep-lat].
- [115] U. Wolff (ALPHA), Comput. Phys. Commun. **156**, 143 (2004), [Erratum: Comput.Phys.Comm. 176, 383 (2007)], arXiv:hep-lat/0306017.
- [116] G. Bergner, T. Berheide, G. Munster, U. D. Ozugurel, D. Sandbrink, and I. Montvay, JHEP **09**, 108, arXiv:1206.2341 [hep-lat].
- [117] S. Ali, G. Bergner, H. Gerber, P. Giudice, I. Montvay, G. Münster, S. Piemonte, and P. Scior, JHEP **03**, 113, arXiv:1801.08062 [hep-lat].

- [118] A. Cheng, A. Hasenfratz, G. Petropoulos, and D. Schaich, *JHEP* **07**, 061, arXiv:1301.1355 [hep-lat].
- [119] G. Lepage, B. Clark, C. Davies, K. Hornbostel, P. Mackenzie, C. Morningstar, and H. Trotter, *Nuclear Physics B - Proceedings Supplements* **106-107**, 12 (2002).
- [120] W. I. Jay and E. T. Neil, *Phys. Rev. D* **103**, 114502 (2021), arXiv:2008.01069 [stat.ME].
- [121] J. Frison, (2023), arXiv:2302.06550 [hep-lat].
- [122] S. Borsanyi, S. Durr, Z. Fodor, C. Hoelbling, S. D. Katz, S. Krieg, L. Lellouch, T. Lippert, A. Portelli, K. K. Szabo, and B. C. Toth, *Science* **347**, 1452 (2015).
- [123] A. Athenodorou, E. Bennett, G. Bergner, D. Elander, C. J. D. Lin, B. Lucini, and M. Piai, *JHEP* **06**, 114, arXiv:1605.04258 [hep-th].
- [124] B. Lucini and M. Teper, *JHEP* **06**, 050, arXiv:hep-lat/0103027.
- [125] A. Gonzalez Arroyo and C. P. Korthals Altes, *Nucl. Phys. B* **311**, 433 (1988).
- [126] D. Daniel, A. Gonzalez-Arroyo, C. P. Korthals Altes, and B. Soderberg, *Phys. Lett. B* **221**, 136 (1989).
- [127] D. Daniel, A. Gonzalez-Arroyo, and C. P. Korthals Altes, *Phys. Lett. B* **251**, 559 (1990).
- [128] R. C. Brower, H. Neff, and K. Orginos, *Comput. Phys. Commun.* **220**, 1 (2017), arXiv:1206.5214 [hep-lat].
- [129] A. Hasenfratz, Y. Shamir, and B. Svetitsky, *Phys. Rev. D* **104**, 074509 (2021), arXiv:2109.02790 [hep-lat].
- [130] A. Athenodorou, E. Bennett, G. Bergner, and B. Lucini, Investigating the conformal behaviour of SU(2) with one adjoint dirac flavor — data release, doi:10.5281/zenodo.5139618 (2021).
- [131] A. Athenodorou, E. Bennett, G. Bergner, J. Lenz, and B. Lucini, SU(2) gauge theory with one and two adjoint fermions towards the continuum limit — analysis workflow, doi:10.5281/zenodo.12802810 (2024).